Chapter 6

Electromagnetic Calorimeter

6.1 General Overview

The decision to use a high-performance crystal electromagnetic calorimeter in BTeV was driven by the physics goals of the experiment, that generally are to make complete studies of CP violation and rare decays of b-flavored hadrons. This chapter describes general requirements arising from these physics goals, design of the calorimeter and its rationale. The design is supported by several years of R&D activities carried out by the Electromagnetic Calorimeter (EMCAL) Group of the BTeV Collaboration.

A thorough investigation of B decays requires not only the ability to track and identify charged particles, but also the ability to reconstruct photons. To address many of the physics issues we are interested in studying, we need to disentangle various isospin components of the decays. This inevitably involves decay modes containing π^0's. Detection of neutral pions is critical, for example, in extracting the α angle of the unitary triangle using $B \to \rho\pi \to \pi^+\pi^-\pi^0$ or $B \to \rho^+\rho^- \to \pi^+\pi^-\pi^0\pi^0$. It is also crucial to detect $\eta^{(\prime)}s$ and isolated photons. The decay mode $B_s \to J/\psi\eta^{(\prime)}$ used for the determination of the angle χ involves either $\eta \to \gamma\gamma$, $\eta' \to \pi^+\pi^-\eta$ or $\eta' \to \rho\gamma$. Other important decays involving direct photons are $B \to \gamma K^*(\rho \text{ or } \omega)$. Thus, since much important physics depends on the calorimeter, our goal is to optimize its performance while keeping costs under control.

Total absorption shower counters made of scintillating crystals have been known for decades for their superb energy and spatial resolutions. The crystals act as both the shower development media and scintillation light emitter. Since the entire calorimeter is used to measure the energies of photons, the resolution can be excellent. Lead tungstate (PbWO$_4$ or PWO) crystals are distinguished by their high density (8.3 g/cm^3), short radiation length (0.89 cm), small Moliere radius (2.2 cm) and short relaxation time (15 ns for the major component) as well as its tolerance of radiation. The light output, of 10 photoelectrons per MeV into 2-inch PMT with a standard bialkalai photocathode, is modest compared to many other scintillation crystals, but adequate. These characteristics are a good fit to the BTeV calorimeter. Since BTeV will operate in a very high particle density environment, it is very important that signals from two particles do not overlap in space and time very often. The

smaller the Moliere radius, the more compact are the showers created by photons, and the less frequently do two of them overlap in space. The shorter the scintillation signal, the less likely that two of them overlap in time. (However, there is no particular benefit of having the signal shorter than the time between bunches, as all the particles from a particular bunch crossing are in time.)

The space for the EMCAL is limited in the BTeV experimental hall. The dense nature of the PWO crystals makes it possible to construct a compact calorimeter. The shorter calorimeter gives hadron showers less room to spread out when their parent hadrons interact in the calorimeter, making them less likely to overlap with photon signals. In general, scintillation crystals are radiation sensitive, and the high-radiation environment of BTeV makes it impractical to use them. However, years of R&D studies, much of them done by people in CMS, show that PWO crystals are an exception. Finally, PWO crystals are one of the most economical scintillation crystals, and pure enough crystals which are radiation tolerant can be produced more cheaply than regular (not radiation tolerant) CsI or BGO crystals. These are the major reasons why an electromagnetic calorimeter made of PWO crystals has been selected as the baseline for the BTeV experiment. The CMS [1] and ALICE [2] experiments at the CERN LHC have chosen these crystals for their electromagnetic calorimeters for similar reasons. The EMCAL will consist of about 10,000 crystals, each 28×28 mm^2 in cross section in the back and 220 mm in length. They are slightly tapered in shape so that they can be in a projective geometry where all the crystals are pointing to a place near the interaction point. The projective geometry will secure better resolutions, in particular, position resolution, especially in the outermost area of the calorimeter. In order to avoid lining up gaps between crystals with potential paths of photons, the convergence point is displaced from the IP by 10 cm both in the horizontal and vertical directions.

Unlike CMS or ALICE, the BTeV EMCAL is not situated in a high magnetic field, so we can use photomultiplier tubes (PMTs) rather than avalanche photodiodes or vacuum phototriodes. Fringe field from the toroid gives up to 40 Gauss in the phototubes. Our default assumption is that the field can be significantly decreased by having an 1-inch steel plate backed up by a thin sheet of μ-metal right next to the toroid. Fringe field from the upstream vertex magnet is up to 15 Gauss in the phototubes. A thin sheet of μ-metal can be placed in front of EMCAL to shield phototubes against this field. The use of PMTs give better resolutions at low energies. We expect that approximately 5000 photoelectrons will be produced in a 1-inch diameter bialkali photocathode PMT at 1 GeV. Hereafter we assume that the maximal quantum efficiency of the mentioned phototubes is 25%. Note that for quality assurance (QA) purposes, we refer to photoelectron yield for 2-inch PMT's, that covers the entire end of a crystal being measured, while in the context of crystals being used in the BTeV experiment, we refer to photoelectron yield for 1-inch PMT's; the latter are slightly smaller than the crystals and thus collect less light.

Signals from PMTs will be digitized using FNAL QIE technology, which has evolved from that used in the KTeV, CDF, CMS hadron calorimeters and in MINOS. FNAL is working

on the design of BTeV QIE. It will have a quasi-constant fractional digitization resolution of less than 0.3%, covering a dynamic range of almost 10^5.

Our choice of the PWO technology and our approach to the EMCAL operation over the lifetime of BTeV are supported by an extensive R&D program. These studies yielded many important results, some of them unique. We have good understanding of how crystals will behave over time and whether their light output will fluctuate, for example, due to radiation environment or due to temperature variations. We have designed systems to carefully monitor possible changes. We have also carried out extensive MonteCarlo study to establish EMCAL daily calibration scenario that will employ particles produced in physics data.

In the following sections we will describe each EMCAL component in terms of the requirements, the current design and what we have learned in our R&D studies. Section 2 will list the basic EMCAL requirements set by our physics goals, and the requirements on the PWO crystals. Section 3 will cover the properties of PWO crystals and what we have learned from our test beam and source studies at IHEP, Protvino. Section 4 will describe the PMTs and electronics. This is followed by results from a calibration and monitoring system using actual data as well as precision light pulsers in section 5. The mechanical support structure is covered in Section 6. The assembly procedure, installation in the C0 Hall and integration with other components of BTeV are given in Section 7. Simulation studies of the BTeV EMCAL are given in Section 8. In Section 9 we discuss the R&D studies we still need to do. Finally, we will present our estimate of the cost and schedule in Section 10 and conclude with the EMCAL group organization in Section 11.

6.2 Basic Requirements

The following are the requirements set by the physics goals of BTeV on the performance of the electromagnetic calorimeter. The resolution of the calorimeter is one of the defining characteristics of the system.

- **Detector size**: The system has to provide acceptance for photons of more than 1.3×10^{-2} steradians. In terms of the radius of the calorimeter this corresponds to 1.6 m. The choice was made to reduce the cost by a factor of about 2, while the loss in signal for most final states will be only 20%.

- **Energy Resolution**: The energy resolution of photon showers as a function of the energy is better than $\sigma_E/E = 2\%/\sqrt{E} \oplus 1\%$.

- **Position Resolution**: The position resolution of photon showers as a function of the energy must be better than $\sigma_x = 4\mathrm{mm}/\sqrt{E} \oplus 1\mathrm{mm}$.

- **Radiation Tolerance**: After an integrated dose of 10 Mrad (100 kGy), energy and position resolution should not deteriorate by more than a factor of 2.

Table 6.1: Properties of PWO crystal

Property	value
Density	8.28 g/cm^3
Radiation length	0.89 cm
Molière Radius	22 mm
Interaction Length	22.4 cm
Light Decay Time	5 ns (39%)
	15 ns (60%)
	100 ns (1%)
Refractive Index	2.30
Maximum of emission	440 nm
Light Output(LO)/NaI(Tl)	1.3%
LO Temperature Coefficient	-2 %/C
Light Output (into a 2" PMT)	10 p.e./MeV
Hygroscopic	No
Brittle	Yes

The resolution of this kind of calorimeter is determined by the following factors: the size of the crystals, speed of the signal, and the amount of inactive material between and in front of the crystals. We have requirements on these aspects:

- **Size**: The cross sectional area (the area that the crystals present to incoming photons from the IP area) must be no larger than 28×28 mm^2 to take full advantage of small Molière radius (22 mm for the PWO crystal).

- **Signal Duration**: Signal should decay in 132 ns.

- **Thickness of Inactive Material**: The thickness of inactive material as well as space between crystals must be no more than 1 mm. The inactive materials between crystals and in front of EMCAL should be made of low-Z materials as much as possible.

6.3 Lead Tungstate Crystals

Some of the properties of PWO crystals are listed in Table 6.1.

The crystal-related requirements necessary to accomplish the above general requirements are

- **Light Output**: 10 photoelectrons/MeV into 2-inch PMT with bialkali photocathode.

- **Light Output Nonuniformity**: less than 1%/cm between 3 and 10 cm from the front of the crystal.

- **Signal Duration**: The amount of signal within the first 132 ns must be more than 98% of the signal one collects in 1μs.

- **Size**: The cross sectional area of the crystal is 27.2×27.2 mm^2 in the front and 28×28 mm^2 in the back with a tolerance of $^{+0.00}_{-0.10}$ mm. The length is (220±1) mm.

In the last decade, the production technology of PWO crystals has made significant progress and at least three vendors are now capable of producing them for BTeV. The CMS collaboration has been working during the last several years with the Bogoroditsk Techno-Chemical Plant (BTCP) in Tula, Russia. At present, about 30,000 crystals have been produced by BTCP for CMS. CMS has also been in contact with the Shanghai Institute of Ceramics (SIC) in China in order to develop methods to mass-produce high-quality PWO crystals. SIC has already provided over one thousand PWO crystals for the PRIMEX experiment at Jefferson Lab. In addition, the ALICE experiment has been working with Northern Crystals at Apatity, Russia, to mass-produce PWO crystals. At present about 2/3 of the total 10,800 crystals have already been produced. Beijing Glass Research Institute (BGRI) also has provided a few PWO crystals to BTeV. The three vendors that we are confident can produce the BTeV crystals are BTCP, Apatity and SIC. (It should be noted that SIC produced thousands of CsI(Tl) crystals very successfully for BaBar.)

We have studied sample crystals from these four potential vendors to

- compare their light outputs with the nominal value of 10 photoelectrons/MeV for 2-inch PMT.

- demonstrate that we can obtain the expected energy and position resolutions for photons (or electrons) using these crystals.

- check if their crystals are sufficiently radiation hard to survive the BTeV-like radiation environment (3 krad as a minimum up to 20 Mrad as a maximum over 10 years of BTeV operation as was estimated).

- check if the change in light output can be monitored well enough so that we can maintain good energy and position resolutions over a long period of time in a BTeV-like radiation environment.

- check if these crystals sustain more serious radiation damage when they are exposed to a hadron beam compared with radioactive sources.

- measure radiation tolerance of wrapping materials and glue to join crystals and PMTs.

- decide what is the best way to specify the quality of production crystals based on radioactive source measurements.

Many of these studies have been done at IHEP, Protvino using their test beam facility, which runs twice a year for about a month, once from March to April and once from November

to December. Our Russian collaborators led the program for these studies that included designing and constructing a beam line, measuring the properties of the beam including the momenta of individual particles, constructing the trigger and data acquisition systems and analyzing the data. In addition, IHEP, Minnesota and Syracuse have test benches that were used to measure light outputs of crystals both before and after the beam tests.

From previous studies by CMS collaborators and others, we learned that typical PWO crystals produce about 10,000 photoelectrons per 1 GeV when instrumented with a large enough PMT to cover one of its ends entirely. The stochastic term of the energy resolution arising from statistical fluctuation in the number of photoelectrons will then be $\sigma(E)/E = 1.45\%/\sqrt{E}$, where E is in units of GeV. The effects of shower transverse fluctuations are will result in additional 0.84% contribution in the stochastic term. Overall, one expects the stochastic term of $(1.68\pm0.07)\%/\sqrt{E}$ at 10,000 photoelectrons per 1GeV. There is an additional term in the expression for $\sigma(E)/E$ that is independent of energy, therefore called the "constant term" that becomes dominant at high enough energies. This is caused by (1) shower fluctuations, mostly rear leakage, (2) crystal light collection non-uniformity and (3) calibration precision. Our Monte Carlo studies show that (1) contributes 0.23%. For a typical non-uniformity of our sample crystals (0.5 %/cm in the front part), (2) contributes 0.27%. The issues associated with calibration accuracy is very involved and addressed in Section 5 in detail. For physics simulations we set the total constant term to be 0.55%, somewhat worse than that obtained by KTeV (0.45%).

We also learned from previous studies that

1. current PWO crystals do not sustain permanent radiation damage when they are exposed to photon and electron irradiation (we observed crystal recovery at least up to 98% of the original signal level).

2. PWO crystals suffer less from radiation than most other scintillation crystals [7], and

3. when they are exposed to radiation at a constant rate, the damage does not accumulate indefinitely, but rather the deterioration in light output saturates; i.e. the light output decreases to a lower level but stays constant at that level.

These observations can be explained as follows. Damage occurs in the transmission of scintillation light in the crystal when valence electrons are trapped in metastable states around crystal defects. When this happens, color centers that absorb scintillation light are created because these electrons, which are in higher energy states than the valence band, jump across the band gap by absorbing visible light. The lifetimes of most of these color centers are modest (hours). The color centers disappear when the trapped electrons fall down to the lower-energy states. The lifetimes are quite temperature dependent. This is one of the strengths of PWO crystals and explains observation (1) above. When the rate of new damage production (which is presumably proportional to the dose rate) equals natural recovery rate (which is proportional to the density of damage among other factors), the damage density will reach a plateau, which explains observation (3). When crystals have only a few defects, they are radiation tolerant since as most of the crystal defects are activated

and become color centers, there will be no additional damage no matter how intensive the radiation. Observation (2) is explained by a room-temperature recovery mechanism and low defect densities in the current production PWO crystals. Current mass-production crystals are grown with targeted purification processes to reduce color-center causing defects and with various doping materials to compensate for the effects of lead and oxygen vacancies. (Note that although Molybdenum does not appear to form color centers, it does introduce a long relaxation time ($\approx 1 \ \mu s$) scintillation component and is thus one of the major targets for removal.)

Despite these consistent sets of observations and explanations, we were worried that when these crystals are exposed to hadrons, including neutrons, they may suffer different kinds of damage and thus not survive the BTeV-like environment. Since charged hadrons and neutrons can interact with nuclei and change them to different elements, they can produce new crystal defects. A recoiling particle from the interaction can displace many atoms and produce a cluster of defects. On the other hand, for the crystal defect density created by hadrons to be comparable to that of the typical intrinsic defect density after 10 Mrad of absorbed dose, one must create one crystal cdefect for every 1 keV of energy deposit. This presumably led some researchers in the past to decide that the difference between hadrons and electron/photon radiation would be minimal. Nevertheless we wanted to test experimentally that hadrons and neutrons will not produce accumulating radiation damage. A significant part of our test beam studies of PWO crystals was focused on this issue. The study we carried out with extremely high dose rates (2-3 Mrad in 12 hours), where natural recovery from radiation damage was negligible, showed us that accumulation of damage was still tolerable. The effects of the electron irradiation and the pion irradiation on the overall light output change were quite similar at the same dose rates. This gives us confidence that PWO crystals will be useful over the life of the BTeV experiment.

6.3.1 Test Bench Measurements

Using radioactive sources, ^{60}Co, ^{137}Cs and ^{22}Na, we have measured the light output of sample crystals. These crystals were wrapped with Tyvek. Since most of the crystals were sent to IHEP for test beam studies, many of these measurements were done there, but some of them were done at Minnesota and Syracuse.

The pulse-height distribution of one of the Beijing crystals is shown in Fig. 6.1. The spectrum shown as the dashed line was obtained using an LED light pulser whose intensity was adjusted so that only some of the time one photoelectron is emitted by the photocathode of a Quanticon phototube, which is optimized to observe a single-photoelectron peak. The narrow peak near channel 50 is the pedestal and the next peak near 90 is due to one photoelectron. The spectrum shown as the solid line is obtained with 0.66-MeV photons hitting the crystal from a ^{137}Cs source. The average peak pulse-height corresponds to 4 photoelectrons, but one can see separate peaks due to 1 to 4 photoelectrons. The peaks for 1 and 2 photoelectrons have contributions from the dark-current background of the phototube. Assuming that the average peak position is about 4 photoelectrons/0.66 MeV gamma, we
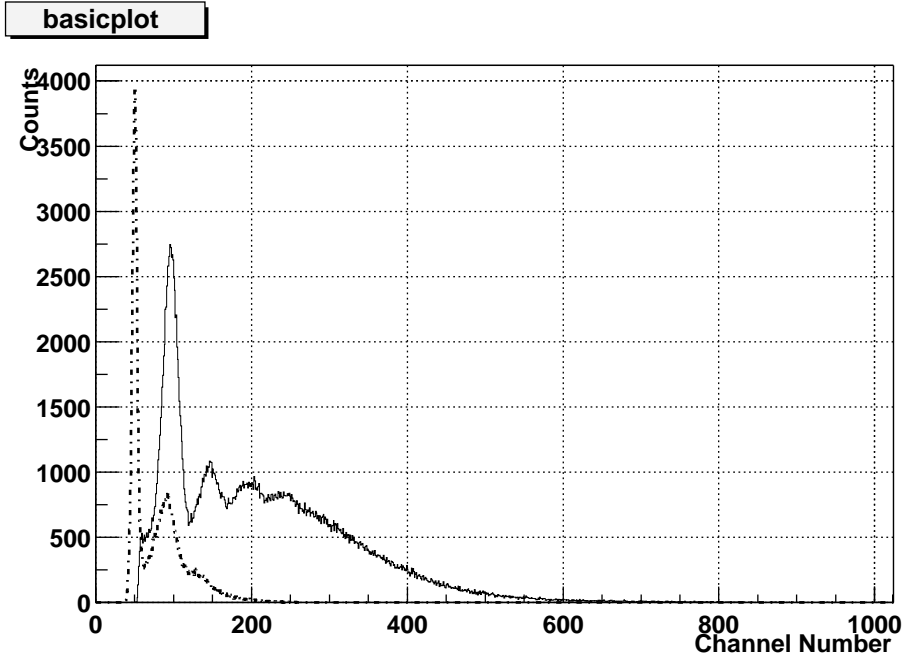
Figure 6.1: Pulse height distribution from a sample crystal using 0.66 MeV photons from a radioactive Cs source. Pedestal, one-photoelectron peak and signal peak are visible. The description of the dashed line is given in the text.

derive that the light output of this crystal is slightly less than 8 pe's/MeV into a 2-inch PMT.

The crystal light yields for some sample crystals from Beijing, Shanghai and Bogoroditsk are shown in Fig. 6.2. The mean is 7.9 pe's/MeV. We found about a 10% variation when we repeated these measurements, and attribute this to the temperature dependence of the background under the single-photoelectron peak. These measurements show that our sample crystals are as good as typical CMS production crystals.

Since the reliability of source measurements will be important in the acceptance testing of crystals, we have solved this problem by using a ^{22}Na source, which produces a pair of 0.511 MeV photons back-to-back. We place a plastic scintillator on one side of the source, opposite from the test PWO crystal and trigger on the signal in the plastic scintillator when we measure the pulse height in the PWO crystal. This virtually eliminates the dark-current background in the large single-photoelectron peak and thus the time variation due to this background. Fig. 6.3 shows the triggered ^{22}Na spectrum measured for one of our sample crystals at Minnesota. The whole spectrum is due to 0.511 MeV photons from the Na source. The prominent peaks due to one and two photoelectrons are consistent with the expectation for a Poisson distribution with an average of 2.8 photoelectrons per absorbed photon. Fig. 6.3 shows the result of a fit assuming that we observe 2.8 photoelectrons from the Na gamma rays. This method provides a significantly more reliable measurement
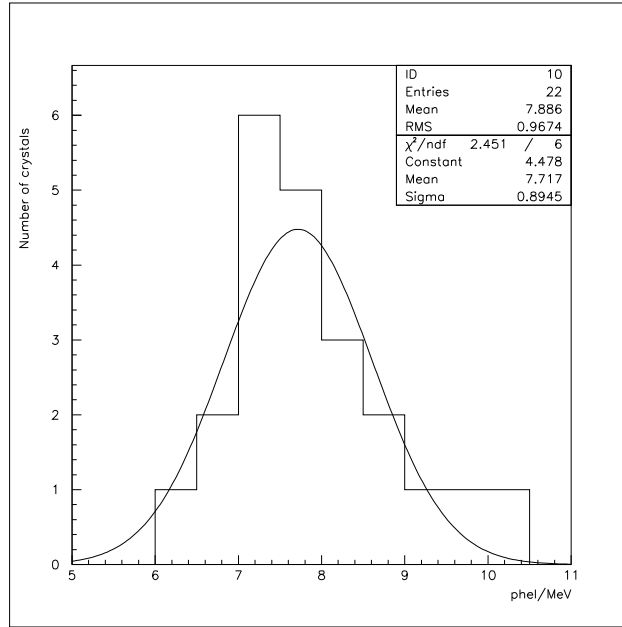
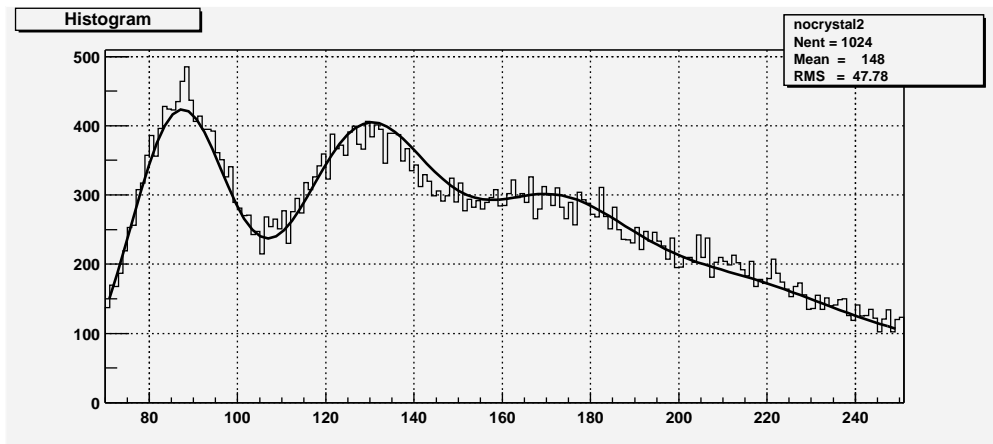Figure 6.2: Photoelectron yields/MeV for the sample crystals.

Figure 6.3: Pulse height distribution obtained with a radioactive ^{22}Na source. The solid line is the result of a fit to the spectrum assuming that the average number of photoelectrons due to the Na gamma ray is 2.8.

Table 6.2: Radiation Tolerance of Optical Glues. Change in transmission after 11 Mrad of irradiation.

Glue	Change	comments
Epo-Tek 302	No change	
Meltmont light	No change	Heat to un-cure
Ock 451	No change	
NOA 81	No change	
NOA 61	No change	
Dow Corning	No change	
Histomont	No change	
Meltmont dark	-1%	Heat to un-cure
Ock 433	-3%	
Epo-Tek 301	-6%	
Epo-Tek 301-2	-7%	
Epo-Tek UVO	-10%	Only 1 Mrad

of the photoelectron yields of the PWO crystals. The difference between the sodium and cesium/cobalt sources is critical when the light output of the crystal is reduced in crystal-quality assurance operations, because here we want to avoid using optical grease to increase the coupling between a tested crystal.

With a source moved along the crystal we measured the light-output uniformity as a function of the distance along the crystal to the phototube end. Most of our test crystals are uniform enough (less than 1%/cm variation over the whole length of the crystal with no tyvek on the both small sides) not to degrade the energy resolution at high energies. Uniformity was also measured at the IHEP test-beam facility using a muon beam passing through the crystals transversely.

In addition to the crystals, the wrapping material should not deteriorate after radiation. Nor should the glue, used to join the crystals and PMT's, lose transparency. We tested three candidate wrapping materials: Teflon, Tyvek and aluminized mylar. Sample materials were used to measure the reflectivity at various incidence angles before and after 10 Mrad of irradiation using a Cs source. We did not observe any measurable changes. The uncertainty of the measurements was estimated to be about 5%.

Similar tests were done with 11 glue candidates. We glued two thin quartz plates with sample glues and measured transparencies using an LED light source and a PMT. We used a control sample, which was not irradiated, to check the stability of the setup. Table 6.2 shows the results of these measurements. Most of the glue samples lost very little transmission.

6.3.2   IHEP Test Beam Facility

Much of R&D studies on PWO crystals have been carried out at the IHEP test beam facility [3] [4]. The main facility provides both electron and pion beams. The energy range of the electron beam is from 1 to 45 GeV, while the pion beam was operated at 40 GeV. The maximum intensity of the pion beam is 10^6 pions/s allowing us to radiate crystals at a rate up to 60 rad/hour. The maximum electron beam intensity is at 27 GeV and was 10^5 electrons/s allowing radiation rates up to 30 rad/hour for the crystal directly hit by the beam. Each beam spill lasted about 1.5 sec of the full accelerator cycle of 9 sec.

The electron beam was used to study energy and position resolutions in addition to electron irradiation studies. The pion beam was used to irradiate crystals at high intensities. This beam has a significant number of muons that were used to monitor the light output changes. An LED based light pulser system was used to monitor PMT gain changes and to study and monitor crystal light loss [11]. A red LED was used to monitor the former while a blue LED was used for the latter, since the crystal transmission for red light is much less sensitive than for blue light.

Since the momentum spread of the electron beam is too large to study the energy resolution of the calorimeter, we installed drift chambers and an analyzing magnet to measure the momentum of each electron.

The BTeV ECAL testbeam setup consisted of a 5×5 array of PWO crystals coupled to ten-stage photomultiplier tubes. Fig. 6.4 shows the inside of the temperature-stabilized (± 0.1°C) light-tight box with its cover removed.

The dimensions of the 25 Bogoroditsk, 25 Shanghai and 12 Beijing test crystals were 27×27 mm^2 in cross section and 220 mm in length, similar to the final BTeV size of 28×28 mm^2 by 220 mm. The dimensions of the four Apatity crystals were 22×22 mm^2 and 180 mm in length (ALICE specifications). All the crystals were wrapped with a 170 μm thick Tyvek. Light from each crystal was measured by a 10-stage 1-inch diameter Hamamatsu R5800 PMT. For resolution studies, we used optical grease to improve optical transmission from crystals to PMTs but for radiation studies, we left an air gap between them because we did not want the issue of optical grease radiation tolerance to complicate our studies. Note that the real BTeV EMCAL will use optical glue between the crystals and the PMTs, and the glue's radiation tolerance has been studied separately.

6.3.3   Resolutions

In the following section we describe briefly our studies of the energy and position resolution of the small PWO calorimeter, using the IHEP test beam. A more detailed description is found in [5].
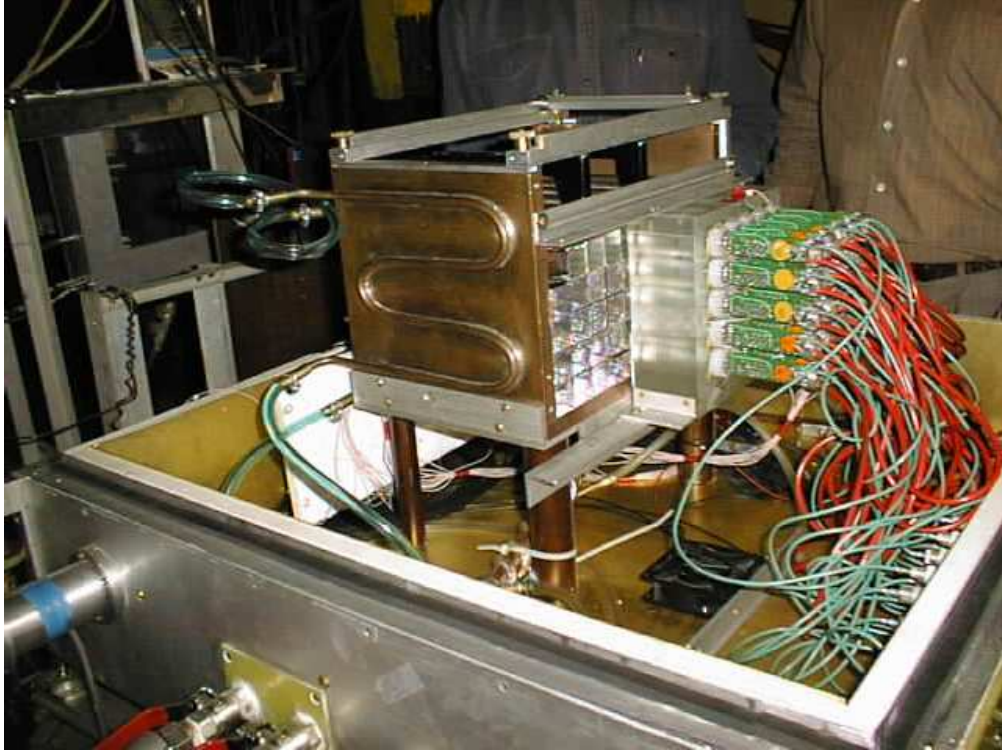
Figure 6.4: View of one of the crystal arrays tested at Protvino. The left half of the crystals have yet to be instrumented. The right half have the PMT's attached as well as the electronics.

6.3.3.1 Energy resolution

We measured the energy resolution of electrons as a function of energy by summing the light outputs of the 5x5 array of crystals. The energies of the electron beam were 1, 2, 5, 10, 27, and 45 GeV.

The energy resolution, σ_E/E, is plotted as a function of E for the 5×5 array of crystals in Fig. 6.5. The data were fit to the function

$$\sigma_E/E = \sqrt{a^2 + \frac{b^2}{E} + \frac{c^2}{E^2}} = a \oplus b/\sqrt{E} \oplus c/E, \tag{6.1}$$

where E is in GeV, $a = (0.33 \pm 0.02)\%$ represents the constant term arising from calibration errors, shower longitudinal leakage, and non-uniformity in the light collection efficiency along the length of the crystals. This agrees very well with our expectation of 0.35%. The stochastic term, $b = (1.8 \pm 0.1)\%$, arises from photon statistics variations and the transverse leakage of shower outside the 5×5 array of crystals. This also agrees very well with the expectation of $(1.68 \pm 0.07)\%$, as calculated assuming 10,000 photoelectrons per 1GeV. The term $c = (2.4 \pm 0.2)\%$ arises from the momentum measurement errors due to multiple scattering of the electrons in the beam line upstream the prototype.
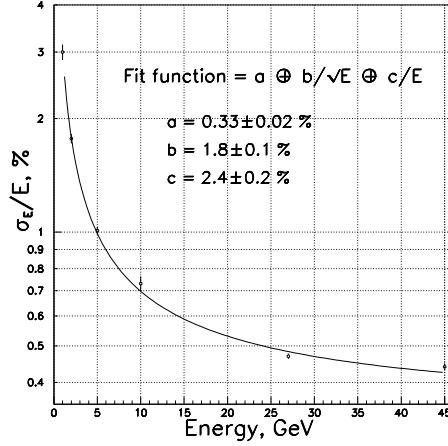
6-12

Figure 6.5: Measured energy resolution of the 5×5 crystal matrix. The curve shows a fit to our experimental results (see text).

We studied the energy resolution for Bogoroditsk crystals and Shanghai crystals by using them in the center of the array, and they performed equally well, given no significant differences in their photon yield and non-uniformities.

The energy resolution shown in Fig. 6.5 was obtained for electrons insident within a small area at the center of the matrix of crystals. If we account for events with the beam hit anywhere within the central crystal of the 5×5 crystal array, including gaps or nearby, the energy resolution σ_E degrades by about 20% at each energy. Increased fluctuations of an energy leakage outside the 5×5 crystal array also contribute to this number. This observation is consistent with MC predictions.

The energy resolutions was also studied as a function of the incident angle.

The prototype was rotated by 5, 10 and 15 degrees relative to the normal. Data were taken with the electron beam of 10 and 27 GeV for each angle.

Both energy and position esolutions as a function of the angle of incidence are given in Figure 6.6. Energy resolution does not degrade significantly until the angle reaches beyond 10°. Effect on position resolution is discussed in the subsection below.

6.3.3.2 Position resolution

From the same data we used to study energy resolution, we obtained position resolution as a function of electron energy. The position of the electron was calculated from the weighted average of crystal positions in the shower, the center-of-gravity (COG), where the weight is proportional to the energy deposit in each crystal. Then it is compared to the position predicted by the beam-telescope drift chambers. The well-known bias in the COG was corrected on a statistical basis. The results are shown in Fig. 6.7. The MC prediction is represented in the figure by the curve that corresponds to $\sigma x = a \oplus b/\sqrt{E}$, where a=(0.17±0.01)mm
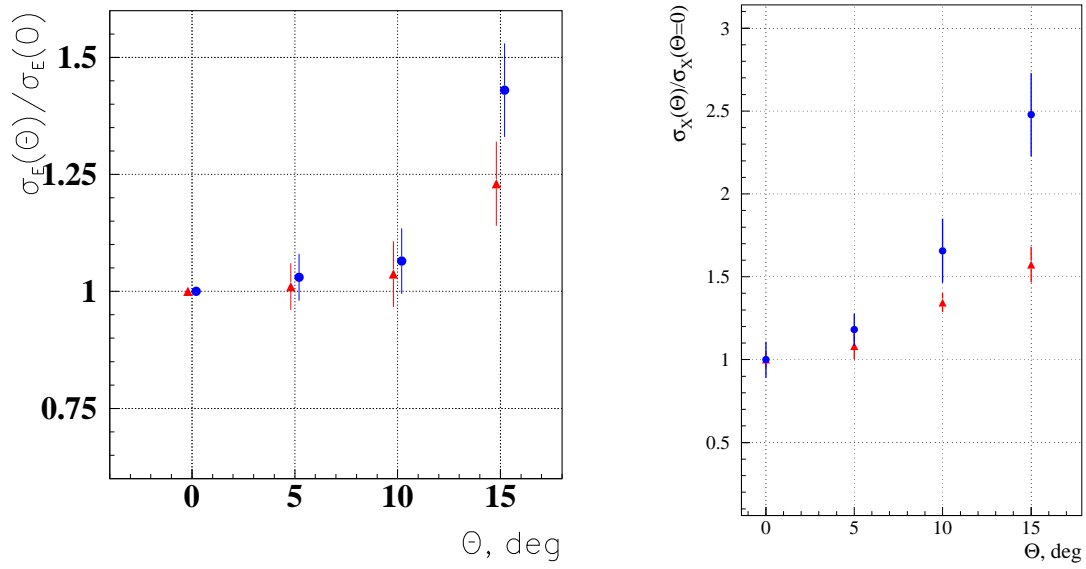
Figure 6.6: Energy (left) and position (right) resolution dependence on the angle of electron incidence. Resolution along the Y-axis is normalized to the resolution at 0°. Circular points correspond to 27 GeV measurements while triangles are for 10 GeV.
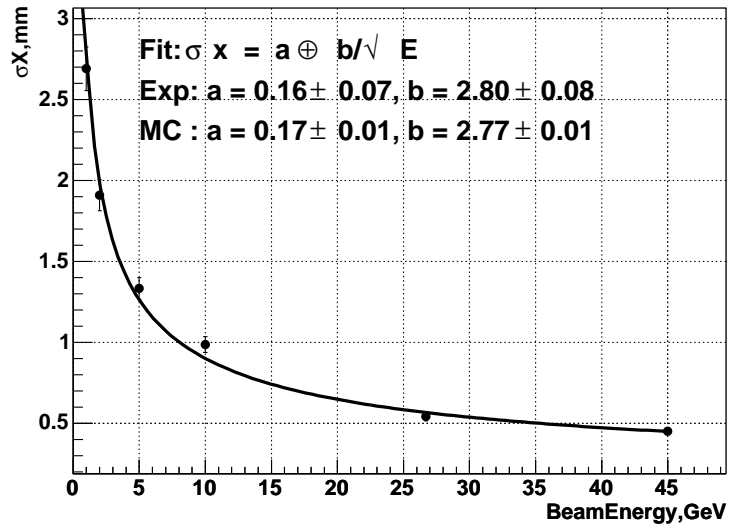

Figure 6.7: Position resolution vs energy. Dots represent the experimental data, and the curve represents MonteCarlo prediction.

and b=(2.77±0.01)mm. A fit of the experimental data to the same function results in a=(0.16±0.07)mm and b=(2.80±0.08)mm. This demonstrates that experimental results are in a very good agreement with the predictions.

Position resolution also strongly depends on where the electron hits the matrix of crystals. The σ_x ranges from ~ 0.28mm near the boundary between two crystals to ~ 0.71mm at the center of the crystal. The effect arises from equal sharing of energies between the two crystals in the former case and minimum energy sharing by the surrounding crystals in the latter.

As mentioned in the previous subsection, we also measured the position resolution as a function of the angle incidence. The results are shown in Fig. 6.6. A significant degradation in the position resolution is evident, especially at angle of $10°$ or higher. This would incude a negative effect on the π^0 mass and energy resolution at high energies, and in turn would affect the B-mass resolution in the decay modes that involve high-energy π^0's. These studies justify that the projective geometry of the calorimeter was the right choice, especially given there is no appreciable additional cost to that.

6.3.4 Light response non-uniformity

GEANT [6] simulations show that a good light response uniformity along the length of the crystal is a key to achieving excellent energy resolution. The non-uniformity of the light yield (LY) along the crystal length contributes to the constant term of the relative energy resolution.

To measure the LY uniformity with the beam, the 5×5 crystal matrix was rotated by $90°$ around the vertical axis and crystals were scanned using a muon beam in 1 cm steps. The position of the muon track going through the crystal was reconstructed using the drift chambers. Pulse-height distributions collected for each of the 1 cm intervals along the crystal lengths were fitted with a modified Landau distribution to obtain a peak position.

The peak position of the energy loss distribution for a minimum ionizing particle as a function of the distance to the PMT is shown in Fig. 6.8. The PMT position is at $X = 0$ cm. The data were fitted in the region of the expected shower maximum (3 to 10 X_0) to a straight line in order to determine the slope of the LY uniformity. The LY values were normalized to the value of LY at $X = 11$ cm. The distributions crystal to crystal look quite different because of difference in the crystals.

A distribution of the slopes of the LY uniformity was obtained for crystals from Bogoroditsk and Shanghai. The results are shown in Fig. 6.9. No difference between the Bogoroditsk and the Shanghai crystals was observed.

6.3.4.1 Temperature dependence of the crystal light output

We made measurements of the temperature dependence of the PWO crystal light output. They were made at electron energies of 10 and 27 GeV. The rate of the temperature change was about 1 °C/hour both during the warm up and the cool down periods. The temperature inside the box was measured using a 24 thermistor array. Their average value was used as
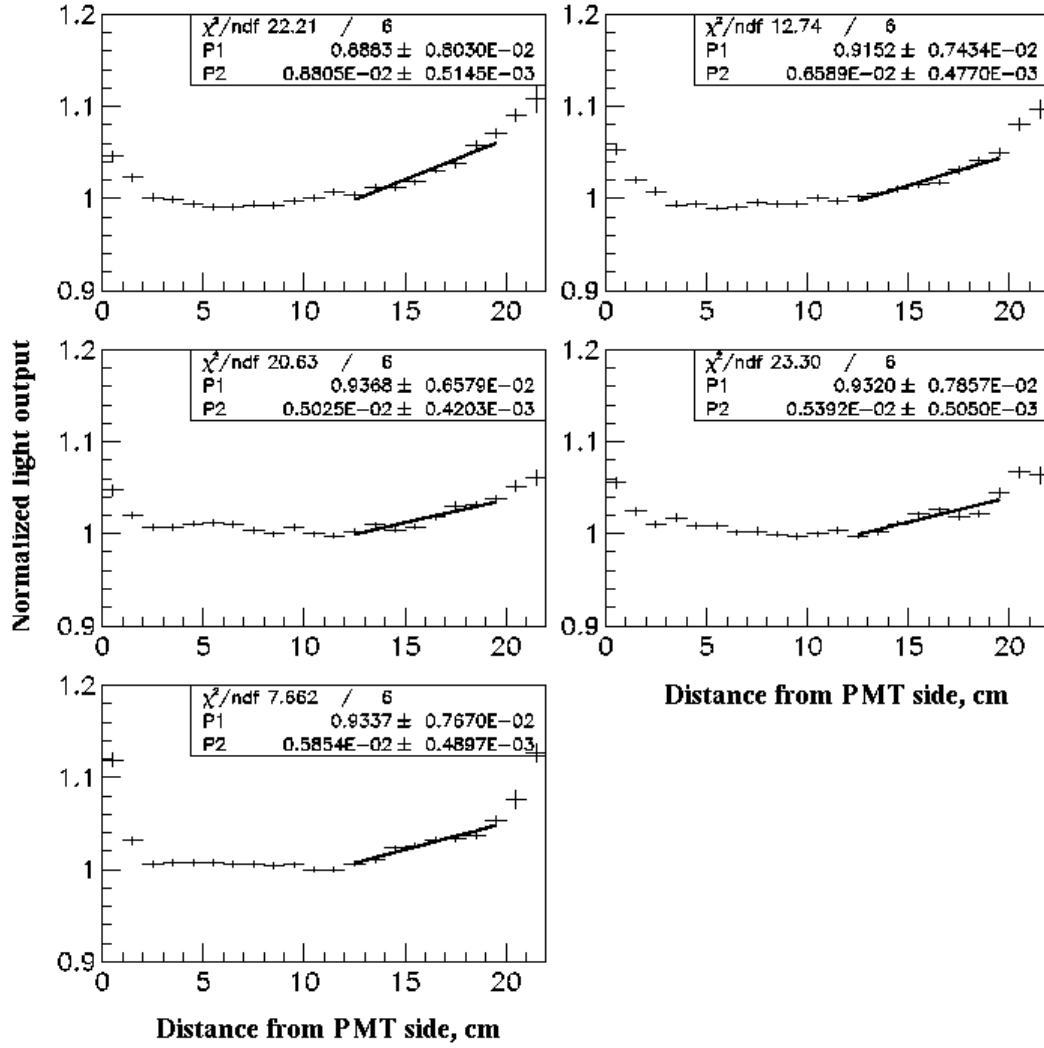
Figure 6.8: Fit results for the energy loss distributions of 5 crystals as a function of the position along the crystal for region 3-10 radiation lengths from the end of the crystal where the electron enters. The PMT position is at X=0 cm. Rise-up at the opposite to the PMT crystal side is due to internal reflection from tyvec. Light yields shown on the vertical axis were normalized to the LY at X=11 cm. Each plot corresponds to one crystal.
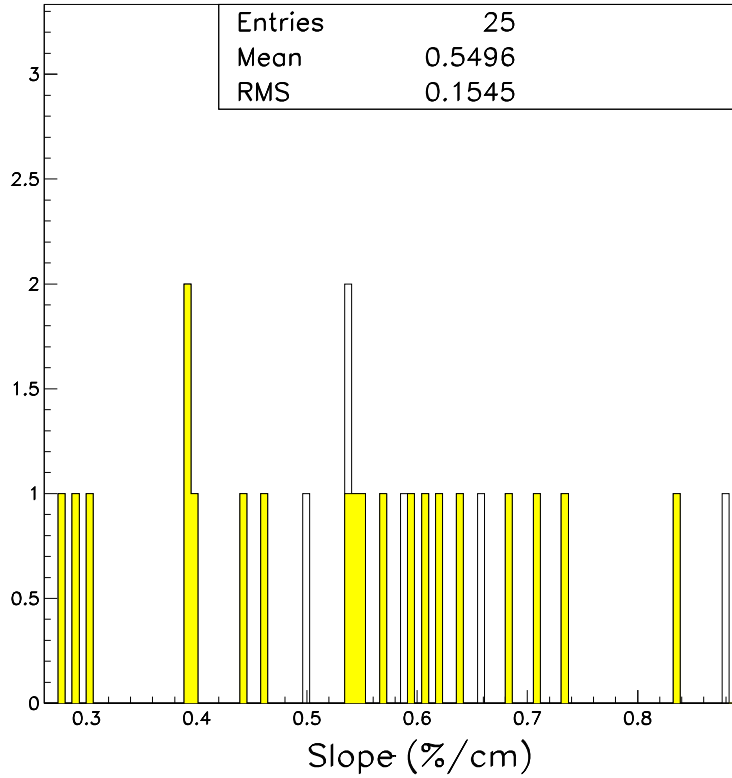
Figure 6.9: The distribution of the LY uniformity slope. The shaded histogram corresponds to 20 Shanghai crystals. The open histogram corresponds to 5 Bogoroditsk crystals.

the "crystal temperature." The temperatures were measured once every spill (approximately 0.1 Hz). The slope of the change in the vicinity of 18 °C was found to be about -2.3% per C, in agreement with previous measurements. Figure 6.10 shows our measurements with 10 and 27 GeV electrons.

6.3.4.2 Study of Potential Scintillation Mechanism Damage

Since no one has evidence of damage to the scintillation mechanism in PWO crystals after irradiation by a gamma-source [7], we have generally assumed that there is none. However, in one of our test-beam studies, we estimated its possible effects by a method suggested by Zhu [8].

We irradiated a small portion of several crystals using a 34-GeV pion beam. The pion beam was directed transverse to the length of the crystals. To estimate the effect of the radiation on the scintillation mechanism, we measured the light-output uniformity with a muon beam, also crossing the crystals in the transverse direction. If only the light-attenuation length (LAL) of the crystal suffers from radiation, the loss of light collection will not be
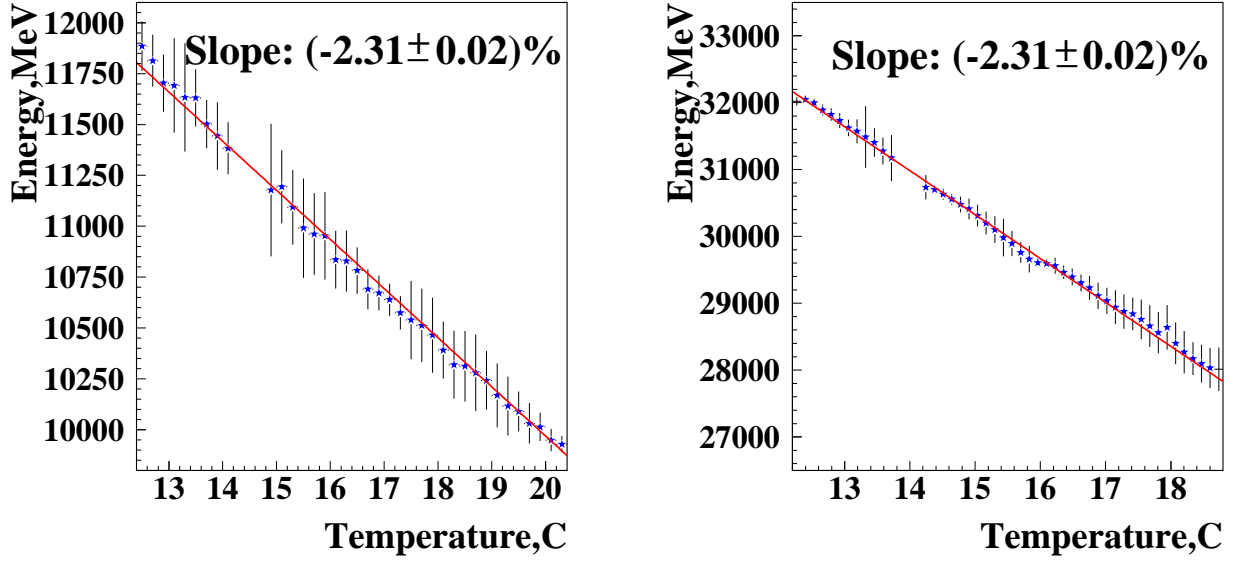
Figure 6.10: Temperature dependence of light output for one of the crystals. Temperature in °C is along the x-axis. Light output in terms of ADC counts is along the y-axis. Measurements were done with 10 GeV (left) and 27 GeV (right) electrons.

localized in the damaged area, since light from other parts of the crystals will also suffer the loss. On the other hand, if the scintillation mechanism (SM) is damaged, only scintillation light produced in the damaged section will suffer. A difference in the measured light uniformity along the crystal length can then allow us to separate the two radiation-damage mechanisms.

For this study, the 5×5 crystal matrix was rotated by 90° around the vertical axis and crystal light outputs were measured using a muon beam before and after irradiation by the pion beam. Two upper layers of the crystal matrix were irradiated by a 34 GeV negative pion beam. The pion beam size was approximately 2 cm horizontally by 6 cm vertically. The beam hit the centers of the crystals along their lengths. The crystals were irradiated for 28 hours with a beam intensity of 6×10^6 particles/spill. This corresponds to an average dose rate of ~ 10 rad/h, for a total of 300 rad.

To measure the light yield along the crystals, the position of each muon track going through the crystal was reconstructed using the drift chambers. Then the pulse-heights from the crystals were recorded, along with the position of the muon. Fig. 6.11 shows the results for a crystal for muons crossing the area of the crystal which was damaged by radiation. One can see clearly that the pulse-height decreased after irradiation. The pulse-height distribution for each crystal was fit for the peaks of the modified Landau distribution in bins of position.

Fig. 6.12 shows the average (peak) light output along the length of one of the crystals, both before and after irradiation. The ratio of the light outputs before and after the irra-
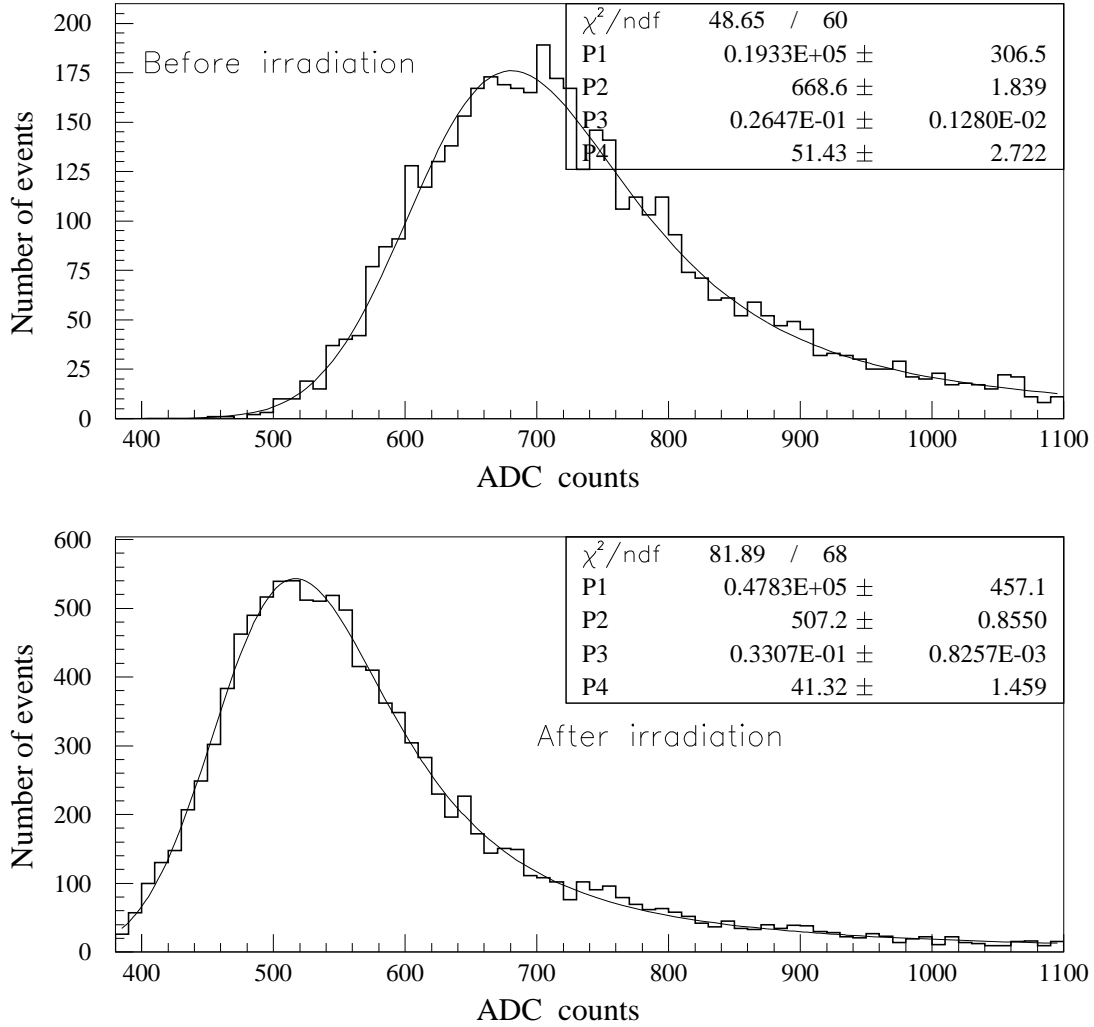
Figure 6.11: The energy-loss distributions and our fits to determine the peak positions for a single crystal, both before and after irradiation.

diation as a function of the longitudinal position is shown in the bottom of Fig. 6.12. The irradiated area is indicated by an arrow. We observe no significant additional light loss in this area, which would indicate damages in the scintillation mechanism. We computed the fractional light loss in the irradiated area relative to the rest of the crystal by calculating the ratio:
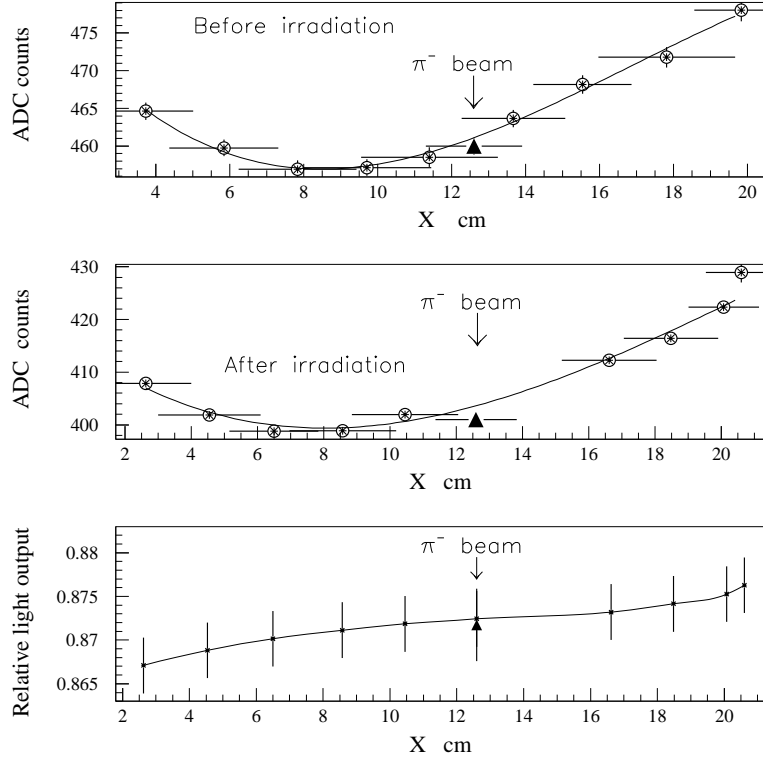
Figure 6.12: The light response non-uniformity before and after irradiation. The last plot shows the ratio of light yields before and after irradiation. Maximum intensity for the irradiating pion beam is at the X=12.6 cm. The PMT position is at X=0 cm.

$$rs = \frac{LO^a(x_\pi)}{LO^a_f(x_\pi)}, \tag{6.2}$$

where the numerator is a Light Output at the pion-beam position x_π measured after the crystal irradiation, and the denominator is the Light Output evaluated from a fit. Index a refers to quantities obtained after irradiation. If rs is unity, there is no localized loss, and any value less than 1 indicates a loss. The values of rs are shown in Fig. 6.13. They show that within our $\sim 1\%$ accuracy we observed no change in the scintillation mechanism.

6.3.5 Radiation Hardness

In this section, we summarize what we learned about the effects of radiation on PWO crystals. We will start with our estimates of the radiation level PWO crystals receive at
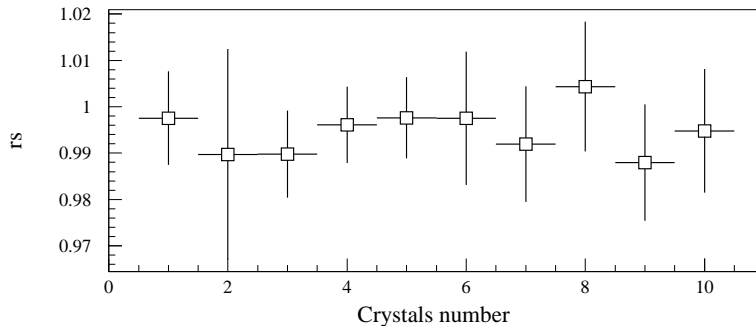
Figure 6.13: The intrinsic scintillation component of the light output change for ten crystals. The first five crystals are from Bogoroditsk and the second five crystals are from SIC and are tapered.

different locations in BTeV, and also at the IHEP test facilities. This study was based on simulations using the MARS code [9]. Then we will discuss results obtained at various radiation facilities: modest dose studies at the test-beam facility with both electron and pion beams, high dose studies at the facility near the U70 accelerator, and radioactive source studies. A more detailed description of the radiation hardness study is given in Ref. [10].

Note that Tyvek wrapping has been shown to withstand the radiation dose delivered in this study. The same applies for the PMT windows, since even regular borosilicate glass does not lose transparency up to at least 10 krad, and quartz glass is unaffected up to 1 Mrad, both within an error of 1%. Six quartz-window PMT's were used for a part of our test beam study, and the rest were borosilicate-window PMT's.

6.3.5.1 Simulation of the radiation environment

The BTeV EMCAL extends outward from the beam line to a radius of 1.6 m. The crystals near the beam pipe receive the highest dose. At the outer radii, the level of radiation is smaller by more than three orders of magnitude. In addition, because the dipole magnet around the primary interaction region sweeps most of the charged particles in the vertical directions, there is much more radiation directly above and below the beam line compared to other parts of the calorimeter. In order to estimate the level of radiation in the crystals we preformed calculations using the MARS code. The estimates of the absorbed dose rates expected in BTeV are shown in Fig. 6.14. The η (pseudo-rapidity) shown here reflects the coverage of the BTeV EMCAL, where η of 4.45 is at the extreme inside near the beam and η of 2.27 is on the extreme outside. Note that the dose was calculated near the "shower maximum" 5-7 cm from the front of the crystals. The fraction of crystals receiving various doses is given in Table 6.3.

Table 6.3: Fraction of crystals with given absorbed doses and dose rates at the maximum of the dose profiles inside the crystals in BTeV (100 rad = 1 Gy)

Relative number (%)	Absorbed dose (krad/year)	Dose rate (rad/h)
11	0.3 - 1	0.11 - 0.36
22	1 - 2	0.36 - 0.72
27	2 - 5	0.72 - 1.8
12	5 - 10	1.8 - 3.6
16	10 - 50	3.6 - 18
6	50 - 100	18 - 36
3	100 - 200	36 - 72
2	200 - 500	72 - 180
0.4	500 - 1000	180 - 360
0.2	1000 - 2000	360 - 720

In the testing facility, we tried to emulate various aspects of the BTeV conditions as much as possible. Both a 27 GeV electron beam and a 40 GeV π^- beam were used to irradiate the crystals with moderate dose rates of 1 to 100 rad/h. Electron and pion dose profiles in the crystals are different; see Fig. 6.14 (c-d). The crystals receive radiation from pions almost uniformly along their length starting from a distance of 5-7 cm from the front. For electrons the absorbed dose rate at shower maximum is two orders of magnitude higher than the dose near the crystal ends.

The difference in the radiation profiles between pions and electrons explains the difference in the radiation profiles in BTeV between crystals near the vertical and horizontal planes. Around the vertical plane, since many charged hadrons are swept into this region by the IP magnet, there are more hadrons. Meanwhile, in the horizontal plane, most of the radiation is due to photons from π^0 decays, so there are not as many hadrons entering this area. As a result, radiation at the rear end of crystals in the horizontal plane is a few orders of magnitude smaller than at the shower maximum. In the vertical plane, meanwhile, much radiation is from hadrons, and radiation at the rear end of the crystals is still substantial. This is one of the reasons why we used both electron and pion beams to study radiation damage of the crystals. We also wanted to verify our assumption that there is no substantial difference in the radiation damage due to electrons and hadrons.

6.3.5.2   Moderate dose irradiation - electron beam

We irradiated an array of crystals for Bogoroditsk, Shanghai, and Apatity with the 27-GeV electron beam for one week. The beam intensity was 10^5 particles/s most of the time during the irradiation. Transverse profile of the beam was bell-shaped, where 90% of the particles
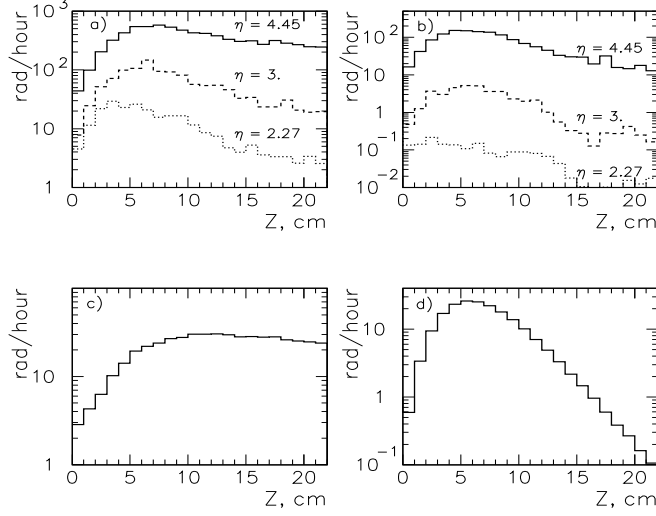
Figure 6.14: Longitudinal profiles of the absorbed dose rate (a) at the vertical plane, and (b) horizontal planes of the BTeV EMCAL at different rapidities, and at IHEP testbeam with (c) 40 GeV pions, and (d) 27 GeV electrons. The length of the crystal is 22 cm. The electron profile is calculated for 10^4 e^-/sec, and the pion profile by $10^5\pi$/sec.

were within a spot of 8 cm horizontally and 6 cm vertically. This means that at a given time a set of 6 crystals received a significant dose, between 12rad/h and 22 rad/h, which corresponds to the dose rate that 80% of BTeV crystals will receive. Other 19 out of 25 in this study received a much smaller dose. We irradiated two sets of 6 crystals one after another, spending about 85 hours at each set, by pointing the beam at different places in the array.

Fig. 6.15 shows typical changes in the light output from a crystal under irradiation, at the average dose rate of 15rad/h. The top plot shows the light output changes over 85 hours. The dose rate profile vs time is shown in the middle plot. The bottom plot shows cumulative dose, which reached 1.2 krad for this crystal. Light output degrades at a faster rate at the beginning of the irradiation; degradation slows down with time and clearly exhibits tendency to plateau, due to self-annealing.

In this study, light output loss in the state of saturation is estimated in the range from ∼5% to ∼12%. In general, it is a function of the dose rate and not of the itegrated dose; however at a given irradiation intensity it may also vary somewhat from crystal to crystal.

Light output degradation under irradiation of constant intensity fits well to the function

$$f(t) = N(1 - a(1 - \exp^{-b \cdot t})) \ , \tag{6.3}$$

where a represents fractional light loss and $1/b$ is the characteristic time that light loss reaches saturation, and t is the time in units of hours.
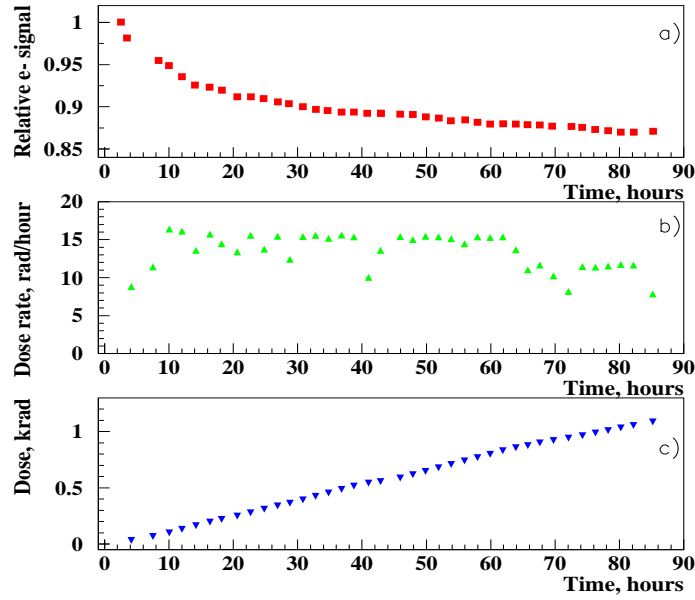
6-23

Figure 6.15: (a) Electron signal in a Bogoroditsk PWO crystal (B14) over 85 hours while being irradiated by 27-GeV electrons. (b) Dose rate. (c) Cumulative absorbed dose.
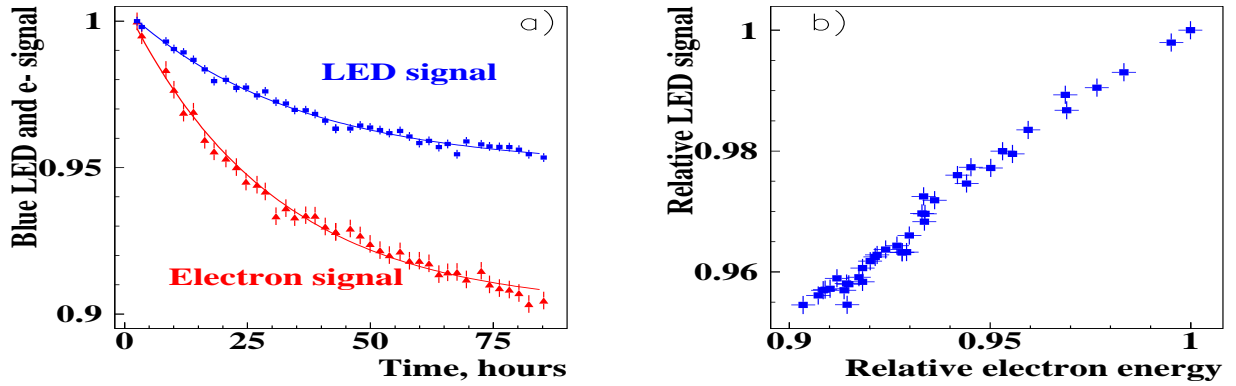

Figure 6.16: (a) Blue LED and electron signal correlation for Shanghai crystal S22, which was irradiated by 27-GeV electrons with a dose rate of 16 rad/hour. (b) Blue LED-electron correlation for the same crystal.

Changes can be monitored by blue LED (wave length 470nm); response to the electron beam and to the blue LED scale well, as shown in Fig. 6.16 for a crystal from Shanghai.

6.3.5.3   Moderate dose irradiation - pion beam

We also studied effect of irradiation by hadrons, with 40GeV pion beam. We wanted to know whether or not :

1. there was a significant difference between effects by hadron, electron or photon irradiation, at the same dose rate;

2. there was a significant damage at higher dose rates since the rate provided by electron beam was limited to 22 rad/h

Crystals were irradiated by the 40GeV pion beam for 4 days. As in the electron irradiation, the transverse profile of the beam was bell-shaped, roughly 8 cm horizontally and 6 cm vertically, with 90% of the paricles within this area. The study was done as a series of runs. Each run lasted for 6 hours. Six crystals were irradiated with a dose rate ranging from 10 to 60 rad/h while other 19 crystals received less than a few rad/h. Irradiation runs alternated by low intensity 27GeV electron beam exposures to measure the light output degradation. We also used pure muon beam to measure the light output, as a cross-check.

We found that, qualitatively crystals behave in a similar way under electron or pion irradiations. They clearly exhibit tendency to saturation at a given dose rate, due to self-annealing. As in the case of electron irradiation, the degree of signal degradation measured in the state of saturation is a function of the dose rate and not of the absorbed dose; also, an exact amount of light output loss in a given crystal is a property of the crystal.

Changes of signal can be monitored by either blue LED, electron beam, or MIP. Response of two crystal to MIP vs absorbed dose is shown in Fig. 6.18(a) and (b). Correletaion between response to the electron beam and to the blue LED during pion irradiation is shown in Fig...; pion irradiation data are represented by dots and agree well with the linear fit. As a reference, this figure also includes similar data taken during electron irradiation, represented by open triangles, that agree well with both data under under pion irradiation and the predictions of the linear fit. This plot demonstrates that crystals behave in a similar way under electron or pion irradiation.

We also studied whether the irradiation induced any changes in the response along the crystal. The array of crystals was rotated by 90° with respect to the beam direction and was scanned with the muon beam. The test was done before and right after the pion irradiation. No signicant changes in the response along the crystals were found, up to the dose rate of 60rad/h (accumulated dose of up to 4krad), even if the irradiation caused light output loss up to 30% in some cases.

This implies that the energy resolution of the crystals will not suffer from radiation-induced non-uniformity.
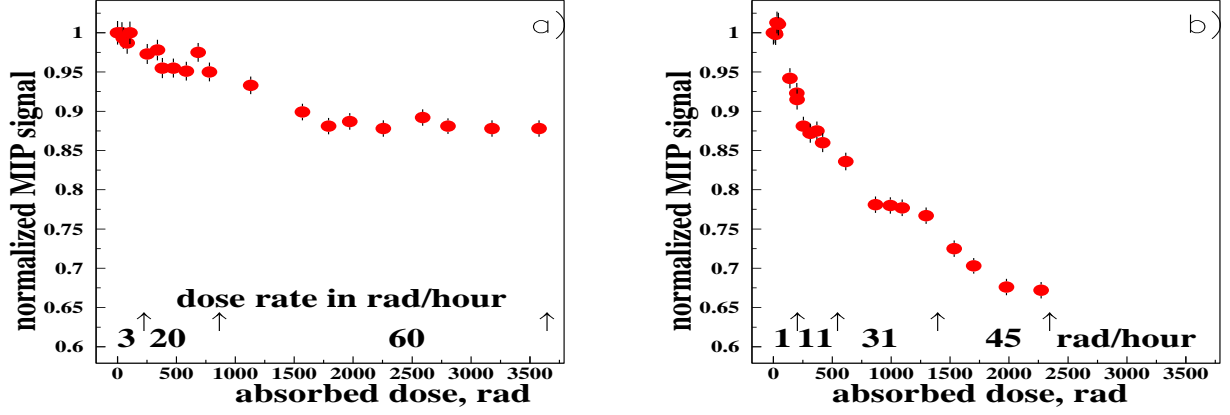
Figure 6.17: Normalized MIP signal vs absorbed dose for Shanghai crystals S16 and S20
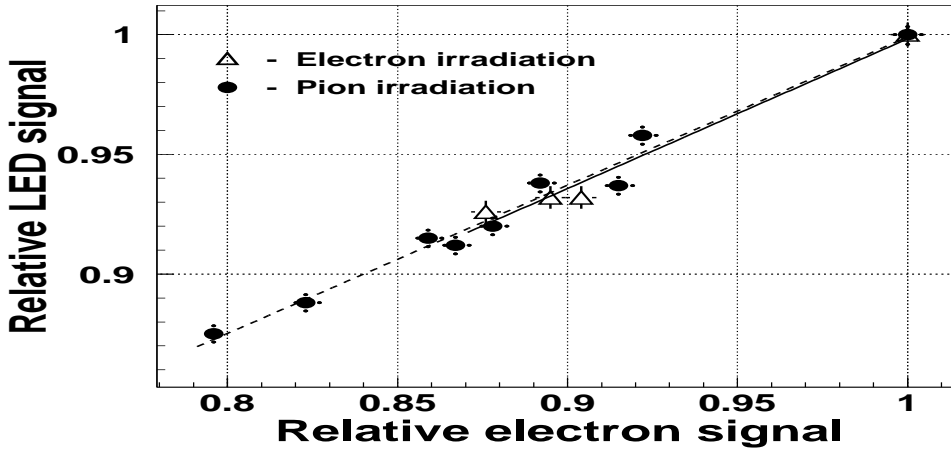

Figure 6.18: Correlation between blue LED signal and electron signal under pion (dots) and electron (open triangles) irradiation.

6.3.5.4 Gamma irradiation - ^{137}Cs source

WE have also done studies to compare crystals light output change under pion and gamma irradiation [12].

Six of the crystals previously irradiated by 40-GeV pion beam with dose rates (30-60) rad/hour were left to recover for over a year at room temperature. Then these crystals were irradiated using ^{137}Cs gamma source at the dose rates (20-100) rad/h. The dose rate profile along the length of the crystal was the same for both irradiation procedures.

Light output loss as a function of an absorbed dose for one of the six crystals under pion and gamma irradiation is presented in Figure 6.19. The behavior of the crystal under two different types of irradiation is similar. Dependence of a signal loss on the absorbed dose under only gamma irradiation for two other crystals is presented in Figure 6.20. Signal
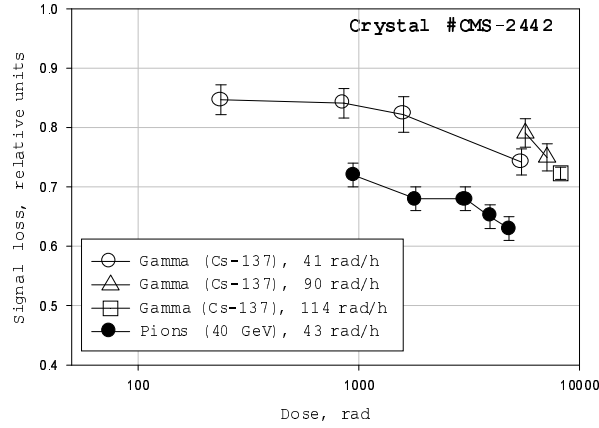
Figure 6.19: Light output loss for the crystal CMS-2442 under pion and gamma irradiation.

degrades rapidly with the absorbed dose up to 100-200 rad, then degrades at a significantly lower rate until the saturation level is reached. Saturation levels are different for different crystals. The same dependence under pion irradiation looks similar.

Ratios of pion/gamma signal losses at the state of saturation caused by irradiation at the same dose rate profiles, for the six crystals are shown in Figure 6.21. These ratios are close to each other and are in the region between 0.8 and 1. One may conclude that pion and gamma irradiation at the same dose rates affect lead tungstate crystals in a similar fashion.

6.3.5.5 Super-intensive beam irradiation

Six crystals from Bogoroditsk and Shanghai were irradiated by secondary particles coming directly from the internal target of the Protvino U-70 accelerator. Two of them, Bogoroditsk B21 and the Shanghai S25, were irradiated at a dose rate of 100 krad/h, and four others, at 1 krad/h. The radiation profile along the length of crystals as well as the composition of charged hadrons, photons/electrons and neutrons in this radiation facility is fairly close to those we will encounter in the BTeV calorimenter. Note also that the cumulative dose of crystals exposed to the higher dose rate of 100 krad/h is comparable to the yearly dose of those few BTeV crystals at the high end of the dose rate range, and to the dose of 10 years worth of running for the top 3 per cent of crystals.

The dose rate was calculated using MARS program and estimated to be accurate to 30%. The calculations were tested by Thermal Luminicent Dosimeters (TLD) and by the ionization chamber measurements at various locations near the crystals. The accuracy of the absorbed dose measurements was estimated to be 30% each. These measurements were in general agreement with the results of the MARS calculations; in the worse case, they differed by a factor of 1.5. The dominant systematic error of the calculations was attributed to the accuracy of the irradiation facility geometry.

These crystals were exposed to radiation in 5 separate rounds, and after each round, we measured the light output of these crystals in the electron beam. Light output losses vs
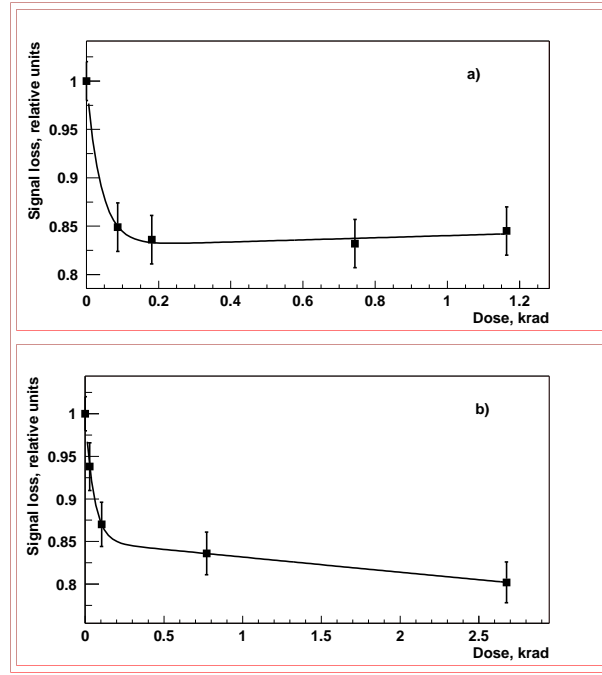
Figure 6.20: Dependence of a signal loss on the absorbed dose under gamma irradiation with a dose rate of 29 rad/h for the two crystals : (a) CMS-2443 and (b) - Bogo2313. Both crystals were produced in Bogoroditsk.
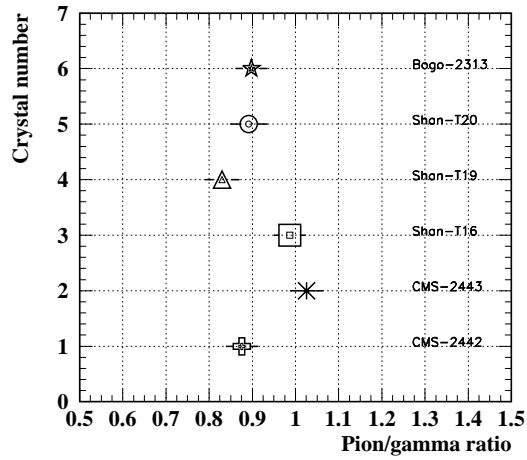

Figure 6.21: Ratios of the two signal losses at their saturation levels, under pion and under gamma irradiation for the same dose rates (30-60 rad/h) for the six crystals.
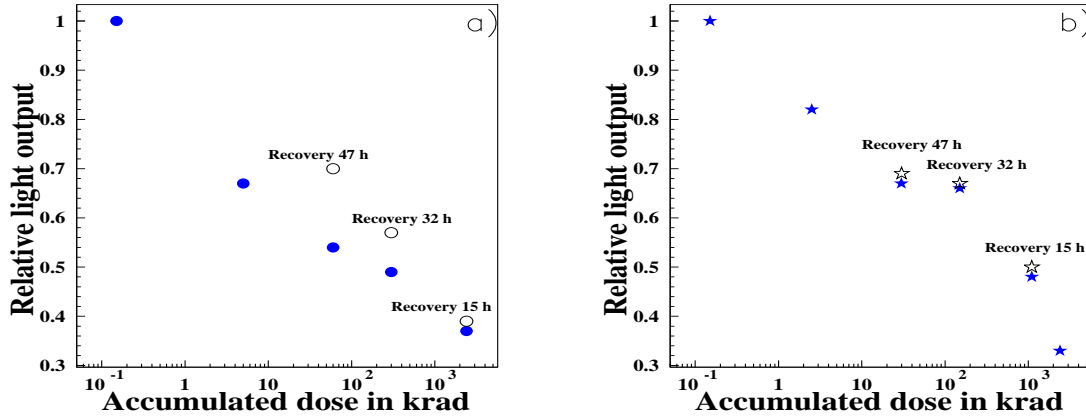
Figure 6.22: Light output changes in the Bogoroditsk crystal B21 (a) and in the Shanghai crystal S25 (b) versus absorbed dose (in krad). Dots represent data taken in the 27 GeV electron beam after immediately after irradiation (100 rad = 1 Gy). Open circles represent signal recovery after specified period of time.

absorbed dose for two crystals, one from Bogoroditsk and one from Shanghai, are presented in Fig. 6.22. Plots include results on signal recovery as well.

One of the most important conclusions is that even after an integrated dose about of 3.1 Mrad and 1.6 Mrad, both crystals remained usable. Even though they lost 2/3 of their light, these severely damaged crystals would form a very respectable calorimeter compared to a calorimeter of any other technologies choice. Note again that we expect only 0.1% of the crystals to receive this much dose in a year and 3%, in 10 years. Most likely, even these few crystals will not suffer radiation damages nearly as severe as these sample crystals since they will have a year to 10 years to recover from the damages while being irradiated.

6.3.5.6 Crystals recovery

After the irradiations by electrons and pions were completed, the HV was kept on the PMT's, to study crystals recovery for ~100 days. Crystals behaviour was monitored with the LED signals. Crystals were found to re-gain their light output, at the level of $(98 \pm 1)\%$ of the signal as it was before the irradiation started. Again, no difference between Bogoroditsk or Shanghai crystals were observed during the recovery. Typical changes of the light output from crystal during the recovery is shown in Fig.6.23, as a function of the recovery time.

6.3.5.7 Conclusions from the test-beam based radiation hardness studies

From this experience we learned several important lessons.

Light output from the crystals degrades under irradiation, at dose rates of 1 rad/h and above. This happens due to formation of so called color centers that affect crystals transparency, as valence electronds get trapped around crystal defects.
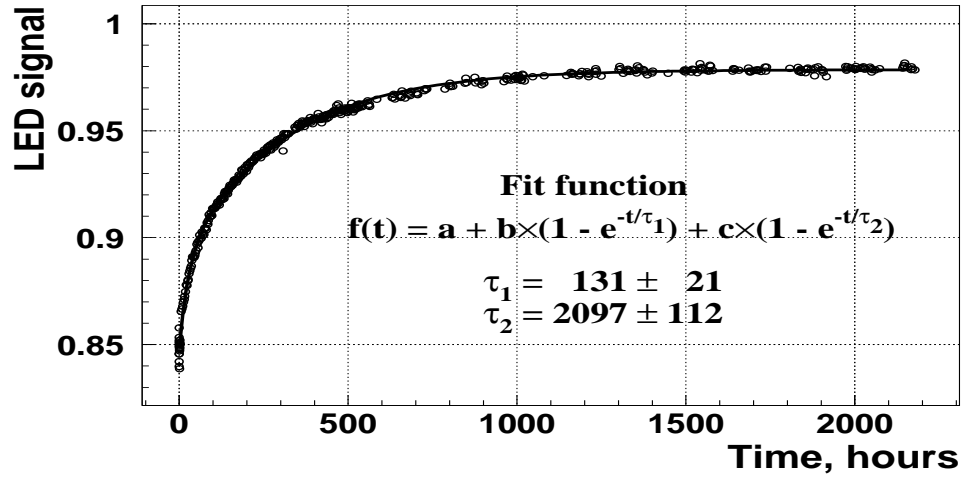
6-29

Figure 6.23: Blue LED signal of the Apatity 1434 crystal which was irradiated by 40 GeV pions for 100 hours and then recovered during the next 400 hours (a). LED damage recovery of the same crystal (b). We see that after 400 hours, the crystal recovered 90% of its light output loss.

Since the color centers are metastable states of varying lifetime and "potential barrieres", crystals are able to recover from the damage (self-annealing), if no longer irradiated or even under irradiation. Because of this, at the beginning of irradiation light output degrades at a fast rate. Then, if the dose rate is constant, self-annealing starts reducing the number of previously created color centers, gradually slowing down light output loss, until at a certain point damage and recovery processes balance each other, thus crystals reach so called saturation. While reaching saturation is a function of the dose rate, an absolute amount of light loss by a particular crystal, as measured in the state of saturation, is also a property of the crystal. This will be taken into account during detector operation.

If left to rest for an extensive period of time, crystals re-gain their light output almost to the level of what it was before the irradiation, i.e. $(98 \pm 1)\%$.

Note that crystals behave in a simular way under either pion or electron irradiation. No damage in the scintillating mechanism due to hadron irradiation was found.

It should also be noted that crystals remained usable even after super-intensive irradiation with the dose rates several orders of magnitude heavier than expected in BTeV.

Monitoring changes in the signal with the blue LED demonstrated that the response to it scales well with the response to an electron beam; linear approximation is good enough to determine the scale between those responses.

However, fluctuations in the light output from crystals during detector operation, as well as some variations in the crystals intrinsic properties, bring up two important issues. First of all, good continuos calibration of the crystals is required. It will be done mainly with electrons produced in physics data. Light monitoring system based on LED's will be used in-between obtaining enough physics data for electron calibration and during shutdown periods.
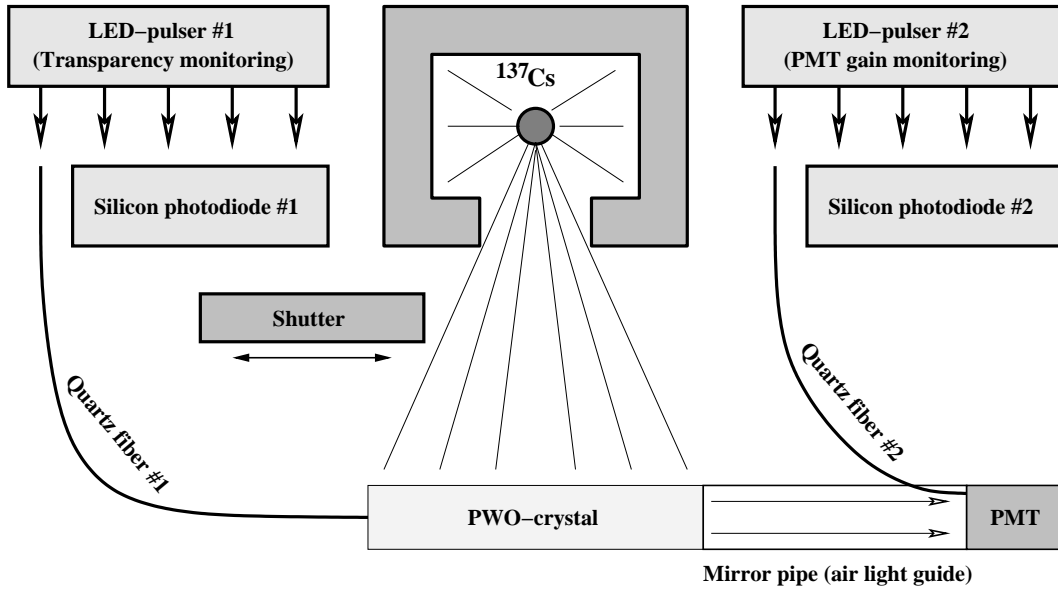
Figure 6.24: Block diagram of the GIF prototype.

Details will be given later in this chapter. Second, good quality control and estimate of the crystals charachteristics before their installation into the calorimeter will also be very useful. Taking into account that pion and gamma irradiation at the same dose rates affect lead tungstate crystals in a similar fashion, it is planned to do this with the gamma-irradiation facility, rather than with the beam, to reduce the cost.

6.3.5.8   IHEP Gamma Irradiation Facility

Gamma irradiation facility (GIF) is a part of the Quality assurance system. The GIF proto-type was designed and installed at IHEP in May 2004. It provides continuous measurements of crystal transparency and light output changes under irradiation using a ^{137}Cs gamma source [12].

The schematic view of the prototype is shown in Fig. 6.24. It consists of the collimated radioactive source with a shutter and a monitoring system, including LED-pulsers, silicon photodiodes, PMT and thermo sensors (not shown) measuring temperature of the crystal, PMT, LED-pulsers and air at the place of irradiation.

The radioactive source has an activity of 5×10^{12} Bq that allows one to irradiate crystals with a dose rate up to 110 rad/hour depending on a distance between the crystal and the source. To avoid unnecessary irradiation of the phototube, a mirror pipe is used as a light guide between the crystal and the PMT photocathode window. Gammas cause intense stintillations in the crystal resulting in permanent photocathode illumination and, thus, a DC anode signal proportional to the crystal's light output. This current is measured in a 1 μsec gate using an integrating ADC.

The crystal transparency change is monitored using the LED-pulser #1. It provides 100 ns light pulses averaged at 470 nm wavelength. The LED-pulser #2 with an LED of 450 nm average wavelength and the same pulse duration is used to track any possible change of the PMT gain. The correction on this signal allows one to extract pure crystal responce on the irradiation. The stability of the light pulse intensities is monitored using the silicon PN-photodiodes.

Light from the LEDs is transmitted respectively to the crystal and to the PMT window through the quartz radiation hard optical fibers. The LED-pulsers are triggered alternatively by a DAQ program. The PMT anode signals from the both LEDs appears at the ADC input in sum with the signal from gamma source. The same duration gate is used for the combined signals charge integration, so the pure PMT response on the LED flashes can be easily obtained in an offline analysis by subtracting a separately measured source signal as a pedestal. The measured source signal itself contains pure pedestal. Its value can be obtained in a dedicated measurement with a closed shutter each time before irradiating a new crystal and then subtracted, assuming that pedestal is stable during the whole irradiation time. It is foreseen nevertheless a remotely controlled blind to be placed in front of the PMT window in a real GIF in order to measure pedestals during the irradiation. The instability of the monitoring system is found to be better then 0.2% over the week.

The GIF prototipe operation is illustrated in Fig. 6.25. The crystal CMS2442 with known radiation hardness properties produced by Bogoroditsk Plant [12] was irradiated using dose rates of 25 rad/h and 100 rad/h. The first 20 hours interval shows the decrease of the crystal light output (Fig. 6.25 a)) and transparency (Fig. 6.25 b)) under dose rate of 25 rad/h. The next 28 hours shows the futher signals degradation at the higher (100 rad/h) dose rate. One can see the recovery process over the last $\sim$ 20 hours when the crystal was exposed to irradiation at 25 rad/h again.

38 crystals (mainly from Apatity) were irradiated with the GIF prototype in the summer 2004. Their light output degradation after 20 hours of exposition at 100 rad/h dose rate is shown in Fig. 6.26.

6.3.6   Crystal Specification

Table 6.4 shows our current idea of PWO crystal specifications. Ideally, we want to measure all the production crystals at a test beam facility to measure the light output, its uniformity along the crystals, the speed of the signal, and the radiation hardness under BTeV-like conditions. The first three are actually easy to measure on a test-bench setup using ^{22}Na source. We will not have enough time to measure the radiation hardness for every crystal using a test beam. So we want to measure various characteristics of crystals from these manufacturers using the test beam facilities at IHEP and FNAL as well as test-bench measurements. From these studies, we expect to be able to find the most sensible specifications for the crystals.

The crystal manufacturers will measure: the crystal dimensions, the absolute light output, the fraction of light in the first 130 ns, the uniformity of light along the crystal, and that the crystal light output does not change more than 5% after exposure to a 15 rad/h source for
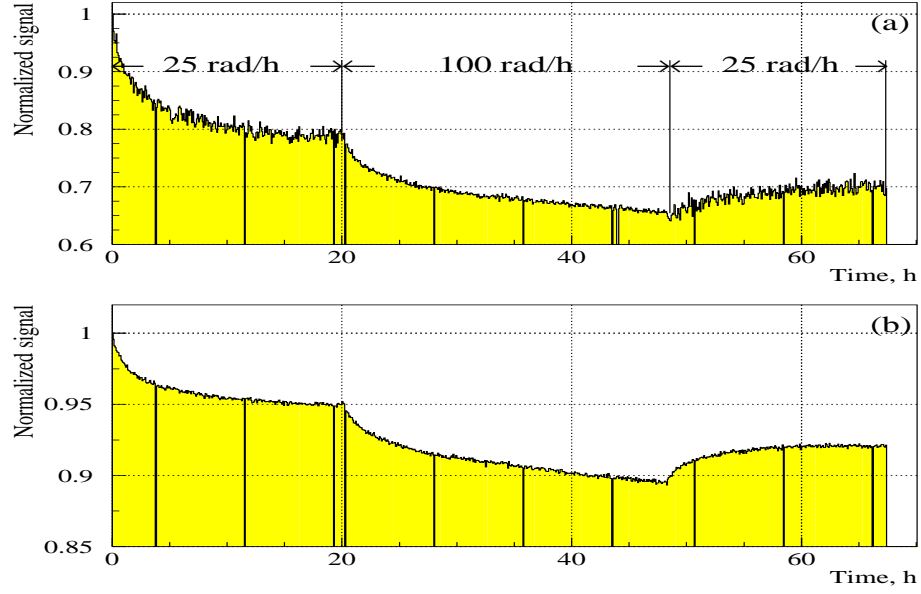
Figure 6.25: Crystal CMS2442 under irradiation with different dose rates: a)light output change; b)transparency change.
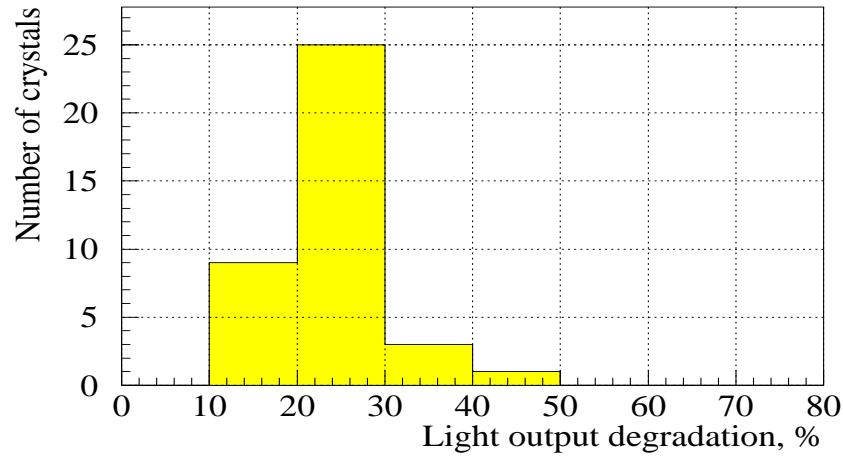

Figure 6.26: Relative light output loss for the 38 set of crystals after 20 hours of irradiatiation at the dose rate of 100 rad/h.

Table 6.4: PWO Crystal Specifications

Average light output	8 photoelectrons/MeV	measured with 2 in PMT with bialkali photocathode
Light uniformity	$< 1\%$/cm	3 to 10 cm from front
Fraction of signal in the first 130 ns/1 μs	98%	
Radiation tolerance	$< 5\%$ change in light output	exposed to 15 rad/hour from ^{137}Cs or ^{60}Co, photons uniformly over the length for 120 minutes
Dimensional tolerance	$+0 - 100$ μm relative to the nominal size	

two hours. BTeV institutions, most likely IHEP in Russia and Nanjing in China will test all of the crystals to make sure that they agree with the manufacturers measurements. Any signifcant differences need to be quicky resolved.

6.4 Photodetectors and Read-out Electronics

6.4.1 Photomultipliers

The BTeV electromagnetic calorimeter is not in the magnetic field. A shielding for fringe fields from the toroid and the vertex magnet is foreseen. Therefore photomultiplier tubes can be used as photo-detectors to detect and measure the amount of scintillation light from individual crystals. The quantum efficiency of the photocathode is one of the most important parameters that affect the performance of the calorimeter. Another important property is how stable the phototube gain is so that we don't have to rely too heavily on the calibration system to correct for these changes. Phototubes must have very low dark current, a few nA. They must be relatively stable. They should have insignificant gain changes when the current changes. They have to be of one inch in diameter to be smaller than the crystal and leave sufficient room for assembly. Photocathode windows have to be tolerant to irradiation.

All the phototubes need to be tested before being used in the calorimeter. The quantum efficiency of the photocathode (cathode sensitivity) and gain (anode sensitivity) will be measured using a standard-intensity light source. The PMT manufacturers will provide these measurements. BTeV institutions will re-measure the same quantities and perform some long term tests on smaller samples. We require 10,350 PMTs including spares.

The PMT must be stable over the life of the experiment and radiation tolerant. Values of the absorbed dose in the phototubes glass windows obtained using the MARS program are presented in Fig. 6.27 and Fig. 6.28.

absorbed doses in EMcal
electronics zone

(vertical plane)

(horizontal plane)

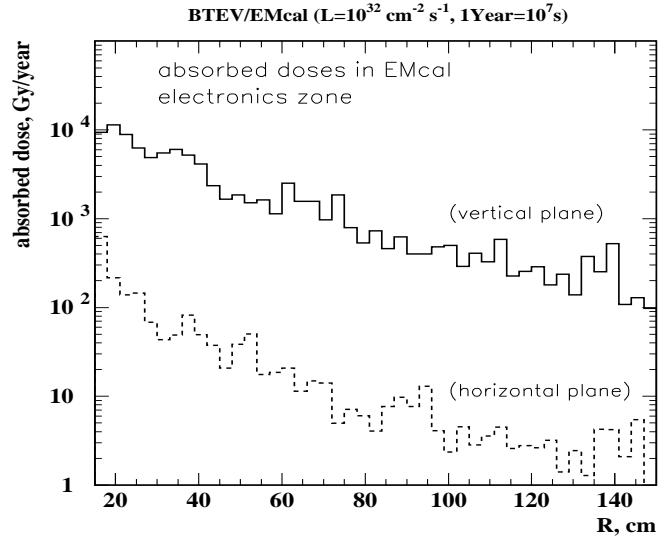Figure 6.27: Absorbed doses in the phototube quartz front window as a function of the calorimeter radius in both the horizontal and vertical plane.

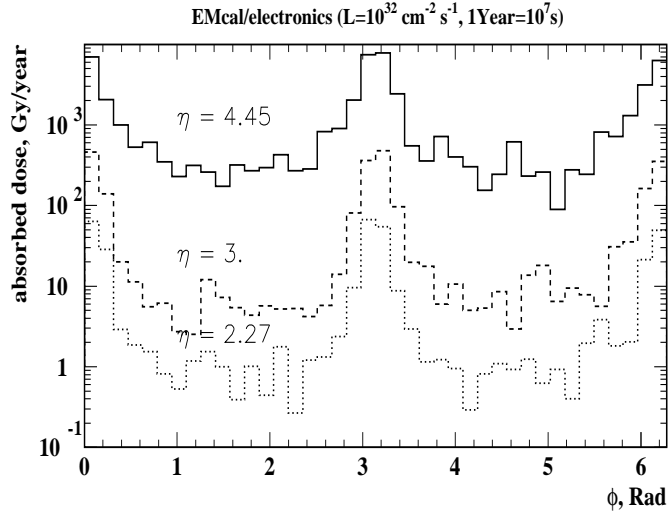EMcal/electronics (L=10^{32} cm^{-2} s^{-1}, 1Year=10^7s)

$\eta = 4.45$

$\eta = 3.$

$\eta = 2.27$

Figure 6.28: Azimuthal profiles of the absorbed dose in the phototube quartz windows. The ϕ-angle is given relative to the vertical axis.

We will run the phototubes at an average output current below 30 μA. Each phototube must meet the following requirements:

- The gain of each PMT must be between 3,000 and 10,000 and uniform over all ∼10,000 phototubes to $\pm 25\%$ when run at the nominal voltage.

- The dynamic range of each PMT must be from 20 photoelectrons up to 10^6 (2 MeV to 100 GeV).

- The gain of each PMT must have a non-linearity less than 2% within the dynamic range of 5×10^4.

- The gain of the each PMT over several hours must be stable to 0.1% given that the HV is stable to 10^{-4}.

- The gain of each PMT over a month must be stable to 0.3%.

- The gain of each PMT over the life of the experiment must be stable to 30% given that the total charge collected by the anode is no more than 100 Coulombs.

There are four potential manufacturers: Burle, ETI, Hamamatsu Photonics and Photonis. They all have long histories of producing quality phototubes. Hamamatsu, for examle, produced the R5380 model, that was successfully used by the KTeV experiment, which had very similar requirements on its PMTs as BTeV. ETI and Photonis delivered several sample tubes. So far, we have found no significant quality difference among these three manufacturers, except that some of the ETI tubes exhibited larger gain variations when the signal rate varies.

6.4.2   PMT gain variations and monitoring

When we started our test beam studies, we did not have a red light pulser to calibrate the gains of PMTs since the KTeV experience suggested that the Hamamatsu PMTs are very stable once the initial burn-in stage is over. (Recall that radiation damage to the crystal will effect blue light transmission but will have virtually no effect on red light.) However early test beam data showed non-trivial gain variation, particularly when the average signal rate changed, for example, when the accelerator went down.

We first investigated this problem at test benches at IHEP and Minnesota. In later test-beam runs, we installed a red LED light pulser system so that we could calibrate the PMT gain continuously.

At the dedicated stand, we studied the PMT gain behavior of pulsed light while varying the average anode current using a DC light shining on the PMT photocathode. Fig. 6.29 shows a sketch of the set up at IHEP.

The setup consisted of a high quality reference PMT (Hamamatsu R5900), a pulsed blue LED with a driver, a DC LED and a PMT that was being tested. LED light was injected into
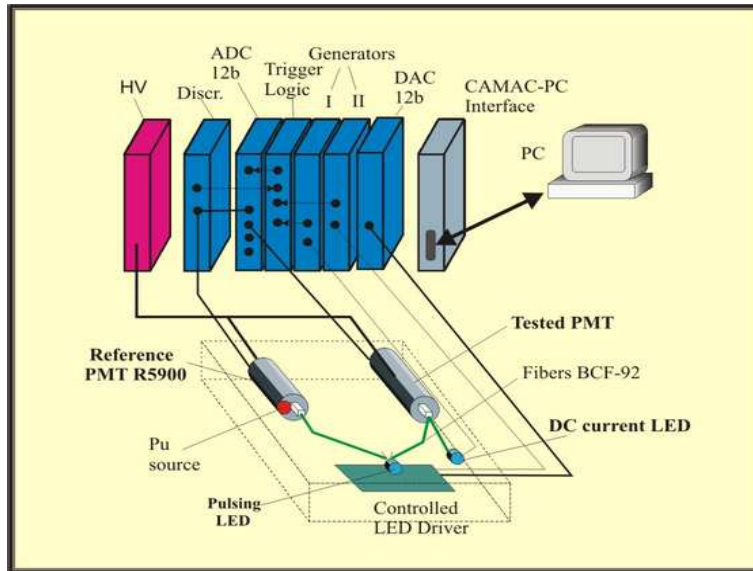
Figure 6.29: Sketch of the PMT gain stability measurement setup.

the test PMT through an optical fiber. The stability of the pulsed LED was monitored by a reference PMT with a Pu radioactive source implanted in a YAP crystal and mounted at the photocathode. The read-out and control electronics were placed in a CAMAC crate which had an interface to a PC. The average anode current was chosen for each test PMT to be about the same as what we had at the test beam. The anode current was measured directly by an ammeter. The average pulse heights from the pulsed LED were measured twice every two minutes. Each measurement contained 2,000 events and took 20 seconds. There was a 10-second time interval between the two measurements. The data from a radioactive source were collected during the remaining 70 seconds. This 2-minute cycle was then repeated. This system allowed us to make long-term PMT gain stability measurements with a precision of 0.2%.

The behavior of PMT 743 is presented in Fig. 6.30. We see a signal loss in the figure when the additional the DC green LED was turned on to produce an anode current of 5 μA. The PMT gain changes due to average anode current variation of several μA were measured for all the PMTs and were found to be less than 3%. Note that some PMT gains increased when the DC light was turned on while many went down. Also, the time dependence of the change varied from one to the next. So it was not possible to correct earlier test beam data reliably for PMT gain changes using these test bench measurements. They were taken into account as a systematic error for our crystal radiation studies of the first two test-beam runs.

Details of PMT gain stabilities and gain monitoring during our test beam studies are described in the Calibration Section in 6.5.2.4. Clearly the behavior shown in Fig. 6.30 is unacceptable. We have been in contact with Hammamatsu and they are confident they can fix this problem. Tubes from other manufacturers have not shown this problem.
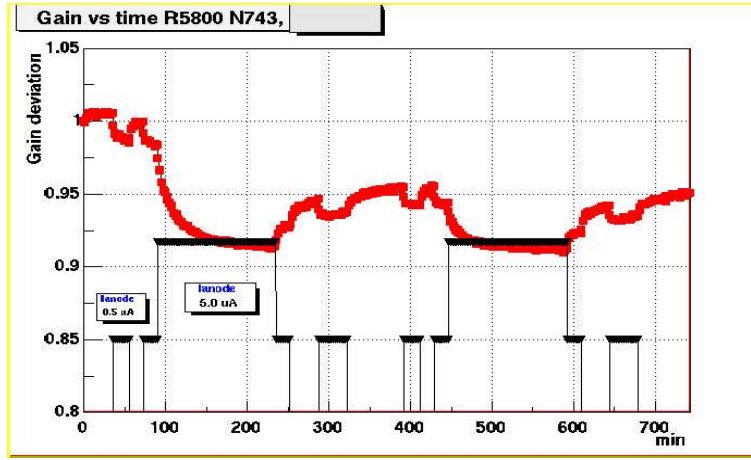
6-37

Figure 6.30: The behavior of PMT 743 at the dedicated stand for PMT gain variation measurements. (See text for details.)

6.4.3 High Voltage Distribution System

The HV system must be able to supply stable voltages and sufficient current capacity. It needs to be separated into multiple channels so that we can control the voltages individually, and monitor the currents to detect various abnormalities. Crystals will be combined in several groups with the same high voltage value for the whole group. Currently, we are assuming that we will have 100 or so HV channels, each serves about 100 PMTs.

Since we are using 6 stage tubes, we can afford to supply 7 separate voltages (including photocathode) and avoid having current drawing voltage dividers. However, cathode through dynode 3 draw much smaller currents than the other 3, we supply HV to them using conventional voltage divider circuit without increasing power dissipation significantly. We will, then, supply 4 separate voltages and generate the remaining three with a divider.

The requirement of the short-term stability of the HV system is that the output voltage must be maintained to 10^{-4} over a week. The Medium-term stability requirement is that the output voltage must be stable over a month to 10^{-3}. Long-term stability demands that the output voltage must be stable over the life of the experiment to 5V. We need to be able to monitor the output voltage of the HV supply to 0.1 V and current draw to 1% of the maximum current.

6.4.4 Front-End Electronics

Analog signals from photomultiplier tubes are sent via copper cables to custom electronics located in 20 electronics sub-racks positioned in racks near the calorimeter. Each Analog-to-Digital Converter (ADC) card, built with the Eurocard 9U x 400 mm form factor, has 32 channels of electronics and there are 16 ADC Cards per sub-rack. ADC cards reside in the front side of the ADC sub-rack and are paired with Cable Transition cards that reside in the back side. PMT signals are received by the Cable Transition Card and are passed to the

6-38

associated ADC Card via dedicated backplane connector pins. This set of electronics digitizes the analog signals from the PMT's and performs zero suppression on the data. The analog-to-digital conversion is accomplished with a QIE9 full-custom application-specific integrated circuit (ASIC) that is a new version in a series known as the QIE (charge Integrating and Encoding) chip developed at Fermilab.

Data generated by the ADC Cards is sent to Data Combiner Boards which concentrate and pass the data on to the remaining portions of the data acquisition system. The Data Combiner Board also provides synchronization signals to the ADC Card and provides a path for signals implementing slow control and monitoring functions. Communication between the ADC Cards and the Data Combiner Boards is implemented with 500 Mbps serial links over copper cable. Communication between the Data Combiner Boards and the data acquisition system is implemented with 2.5 Gbps serial links over fiber optic cable. ADC Cards (variable numbers depending on the occupancies in the cards) will connect to one Data Combiner Board. The Data Combiner Boards are located in sub-racks in the collision hall.

The new version of the FNAL-developed QIE ASIC will be used to digitize signals from the PMTs. The QIE IC must be robust and easy to test, and must facilitate testing and monitoring of the crystals and PMT's.

6.4.4.1   Electronics Requirements

The following describes the requirements on the EMCAL electronics.

1. Dynamic Range

   For PMT's with a gain of 3000, the signal from PMT's will be 0.6×10^5 to 2.1×10^9 electrons, or 10 fC to 3.4×10^5 fC. Considering variations in the quality of crystals and PMT's, the electronics must have a dynamic range of at least 3.4×10^4 with a preferred dynamic range being 10^5.

2. Electronics Noise

   The system must be designed to keep total noise well below 10 fC. This total noise must include not only intrinsic noise of the QIE IC and other circuitry, but also pick-up noise.

3. Electronics Speed

   The electronics must be able to both acquire signals from PMT's and complete readout on average at the maximum beam bunch crossing rate of 132 nanoseconds.

4. Crosstalk

   Crosstalk must be less than 2%.

5. Some other electronics requirements

   Each calorimeter hit must be given a correct timestamp that identifies the beam crossing number. The QIE IC or Front-End Board electronics need to contain the time

stamp generator. This generator could be located further downstream, perhaps in the Data Combiner Board. All the data that can be downloaded or is set on power up or reset must also be readable. These data includes internal QIE IC capacitor identities.

6. Radiation Tolerance

ADC's and QIE chips in particular will be exposed to up to 5 krad of radiation over 10-year period. They must continue to operate after such radiation exposure.

6.4.4.2 QIE ASIC

The QIE has been designed to digitize negative going signals from phototube bases that have been transmitted over three to five meters of cable. The current pulse from the phototube is best modeled as a pulse which rises to a peak in 1.5 ns, then falls as a sum of three exponentials :

$$I(t) = A[0.39\exp(-t/5\text{ns}) + 0.60\exp(-t/15\text{ns}) + 0.01\exp(-t/100\text{ns})]. \tag{6.4}$$

The specifications on the QIE are listed below.

- The dynamic range of the QIE IC must be a minimum of 3.4×10^4 with a preferred dynamic range of 10^5. If PMT's with a gain of 3000 are used, the signal from the average PMT that needs to be measured will range from 0.45×10^5 to 1.5×10^9 electrons, or 7 fC to 1.9×10^5 fC. If a dynamic range greater than 3.4×10^4 is achieved, the least count should be reduced. In order to deal with variations among crystals and PMT's, it is desirable to have minimum charge of 5 fC.

- QIE input analog signals, much larger than the range of interest, will occur at a low rate. The QIE designer must specify any off-chip protection circuitry required. The QIE must recover from very large signals in less than 1 μsec.

- The QIE must be able to both acquire signals from PMT's and be able to be read out on average at the maximum beam bunch-crossing rate of 132 ns. The QIE must also be capable of operating at a beam bunch-crossing rate of 264 or 396 ns.

- In order to be able to measure energy resolution to less than 0.5%, the QIE IC digitization precision must always be better than 0.15%.

- All QIE IC digital input and output signals must be both differential and LVDS compatible.

- Upon power-up, the QIE IC shall be operational at the default setting once the QIE IC Clock input is active and the QIE IC reset input has been asserted.

- The QIE must be designed so that testing using a DC current source can yield a calibration that will be accurate to better than 0.3% for photomultiplier input.
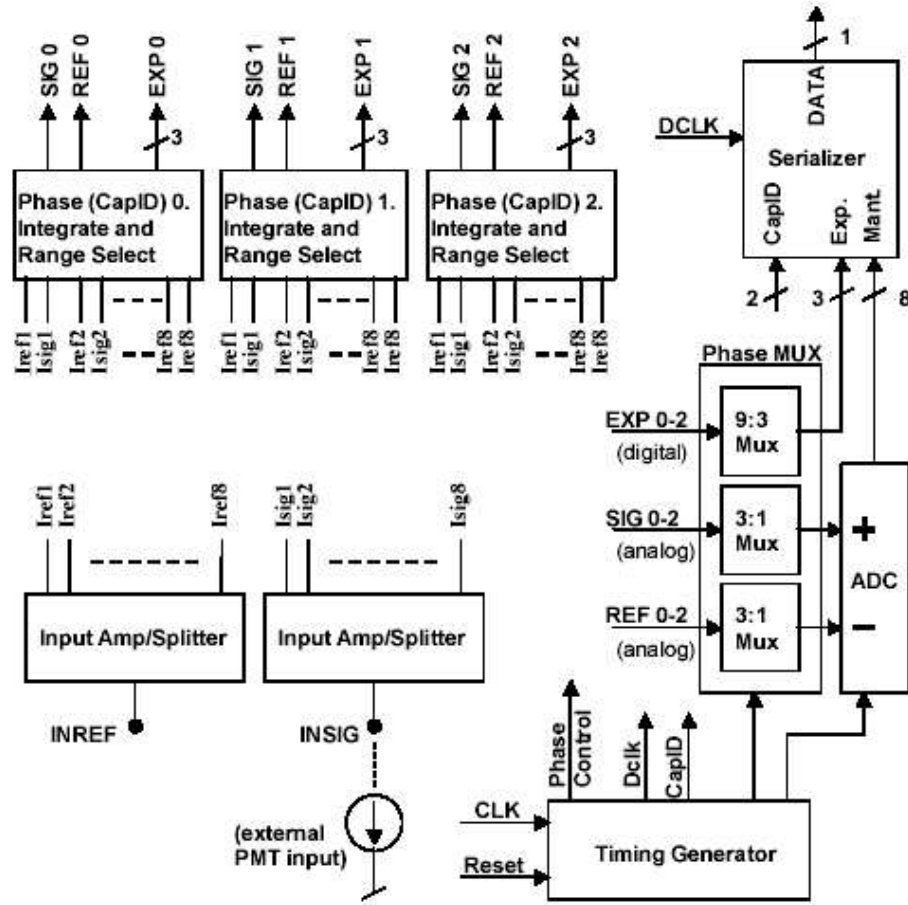
Figure 6.31: QIE9 block diagram

- At the nominal luminosity of 2×10^{32}, the QIE is expected to be exposed to a total dose of approximately 500 rads/year (5Gy/yr). The flux of neutrons with energy between 0.025 eV and 14 MeV is expected to be approximately $10^5/\text{cm}^2/\text{sec}$. The QIE must continue to operate without significant performance degradation after a total dose of 5 krad (10 years operation).

- It is strongly preferred that an ADC with an integral nonlinearity of less than 0.5%, and otherwise capable of meeting all the QIE signal acquisition and readout requirements above be included internal to the QIE.

The QIE9 chip, designed for the BTEV experiment at Fermilab, is the latest addition to a number of various QIE chips developed for high energy physics experiments. A basic block diagram is shown in Fig. 6.31

QIE9 is designed to integrate large dynamic range negative input pulses from a photomultiplier tube (PMT) in 132 ns buckets, and digitize the results with approximately constant

Table 6.5: QIE9 Range Spans

QIE9 range number	ADC count span	Input Charge (fC)	Input Charge per ADC bin (fC)	Resolution (bottom of range),%	Resolution (top of range),%
0	2-240	0 - 1190	5	–	0.12
1	2-240	1190 - 3570	10	0.24	0.08
2	2-240	3570 - 8330	20	0.16	0.07
3	2-240	8330 - 17850	40	0.14	0.07
4	2-240	17.9k-36.9k	80	0.13	0.06
5	2-240	36.9k - 75k	160	0.13	0.06
6	2-240	75k - 151k	320	0.12	0.06
7	2-255	151k - 314k	640	0.12	0.06

resolution over the entire range. It accomplishes this by simultaneously integrating a portion of each input charge pulse on 8 ranges with sensitivities that differ by factors of 2, and then selecting the one appropriate range to digitize based on the signal magnitude. The appropriate integrator output is fed to a custom on-chip 8-bit FADC which digitizes the result. Eight non-overlapping ranges combined with an 8-bit FADC yields a dynamic range of 16 bits.

In order that the QIE9 can integrate and digitize each 132 ns bucket in deadtimeless fashion, all operations are pipelined. Three identical phases of integrators ("capIDs") exist so that digitization and reset can proceed on one phase while the others are accepting input charge. An externally applied input clock (CLK) determines the timing and period of the integrations.

The digital output is composed of an 8-bit mantissa, a 3-bit exponent (range number), and a 2-bit capID to identify which set of integrators generated the data. The data is output serially on one set of LVDS output pads (DATA). The serial output stream is controlled by an externally applied data clock (DCLK), which must be synchronized with the input clock (CLK). The frequency of DCLK should be 14 times the frequency of CLK in order to clock out 14 data bits for each integration clock period (one spare bit, 8 mantissa bits (LSB first), 3 exponent bits, and 2 capID bits). The data latency is 3 clock periods, i.e., when a given integrator phase is accepting input charge, the data that was acquired by that phase 3 clock periods ago is being read out. Table 6.5 specifies the nominal integrated charge and resolution for each of the 8 ranges.

QIE9 is a pseudo-differential device, meaning that in addition to the "signal" input (INSIG), there is also a "reference" input (INREF). A negative input signal current is applied between INSIG and ground, and INREF serves as an identical looking dummy, which helps to cancel any externally induced noise. Inside the QIE9, the outputs of the signal and

reference integrators are routed to a pseudo-differential FADC. Therefore variations in bias, temperature, etc., are a form of common mode noise and have little effect on the signal.

The input impedance of each of the INSIG and INREF inputs is desired to be 50 ohms over the entire dynamic range, in order to properly terminate a coaxial cable. For small input currents, the input impedance is determined by the internal feedback amplifier characteristics and amplifier bias current, which is set with an external resistor to the ISET pad. The ISET resistor is chosen to obtain 50 ohm nominal input impedance (the RinSel digital inputs can be used to tweak this impedance on a per chip basis if needed). For larger input currents, the feedback amplifier becomes inactive, and the input impedance is determined mostly by the resistance in series with the signal path. Thus, to keep the impedance at approximately 50 ohms for large inputs, an external resistor (nominally 47 ohms) must be added in series with the input. This resistor must be inside the amplifier feedback loop, so that its contribution is insignificant for small signals. For this reason, an input requires two pins. The signal from the cable is connected to INSIG1, and a resistor connects INSIG1 to INSIG2. The actual signal current then flows through the resistor into INSIG2. Even though the reference input does not see large currents, it uses the same input structure so that it looks as identical as possible to the signal input.

Input resistors must be added in series with the inputs in order to maintain 50 ohm impedance over a wide dynamic range of input current magnitudes. The signal input impedance value in the low current regime is governed by the ISET input amplifier bias current, set with an external resistor. The impedance in the high input current regime (reater than 1 mA) is more dependent on the value of the external series input resistor than on the ISET resistor value.

6.4.4.3   Readout requirements

The output data from the calorimeter shall be only from those cells that are above a readout threshold that can be set in software.

The calorimeter hit data must include the beam crossing number, chip identification number, and the calorimeter hits for that beam crossing. The calorimeter data must have crystal numbers, and pulse height information for each hit.

The data output from most crystals is fairly low, but those crystals near the beam pipe may have a hit in almost every crossing. The calorimeter readout chip shall be data driven, and capable of continuous readout at a minimum rate of 4 hits every group of 32 crystals per 132 nanosecond beam-crossing time.

The 32-channel ADC Card can be populated with up to 16 500 Mbps links or as few as one link. The data output from most crystals is fairly low, but those crystals near the beam pipe may have a hit every crossing. The ADC Cards connected to the crystals nearest the beam pipe will be populated with 16 links. Those servicing the crystals near the circumference will use one link.

The data output from the calorimeter may be lost for rates above certain rates. However,

the loss should be in a fashion that, when the burst of information is over, the system shall return to normal operation without external intervention.

The system must have a means of recognizing and aborting the readout of any chip that has an unusual high volume of data output (e.g. due to oscillation or noise).

6.5 Calibration and Light Monitoring System

There will be three kinds of calibrations in the BTeV calibration scheme. The most fundamental one is to get the energy scale of the signal, *i.e.* ADC counts to GeV conversions. We have studied, using Monte Carlo simulation, how many electrons we can collect in a given time period. The electrons momenta and thus the energy is measured by the bending in the magnetic field. As we will describe below, there will be enough electrons to calibrate the PWO crystals at least every day, and crystals near the vertical axis can be calibrated as often as every hour. The electrons come mainly from photons converted into electron-positron pairs near the interaction region and semileptonic B decays.

Note that the electron-based calibration will be mainly used to track variations of energy scale for each crystal over time, and is not the only way of determining the absolute energy scale. Additional particles, including π^0's, integrated over a longer time will also be used to determine the absolute energy scale by studying the difference between photons and electrons, and the effects of photon radiation by electrons, among other subtleties.

Since our experience suggests that the gains of the PMTs may change appreciably (more than 1%) over a day, or even an hour when the signal rates varies, we need to monitor these changes using a pulser system using both red and blue light. Particle-based calibration will not have sufficient statistical sensitivity for changes over such short time scales.

Finally, since the crystal's light output also varies over a day, or even over an hour when the radiation rate varies quickly, for example when a new fill in the Tevatron starts, this change must be monitored as well, and the blue light pulser will accomplish this.

Section 6.5.1 will describe the result of our Monte Carlo studies of an electron-based calibration, and section 6.5.2 will present our ideas and experiences on light pulser systems to monitor changes in the crystal light output and PMT gains.

6.5.1 Energy Calibration using Electrons

We will calibrate the EMCAL using isolated electrons (and positrons) produced in data. We will rely on the E/p criteria to identify electrons and use their momenta to calibrate the energy scale of the calorimeter.

Precision on the calibration constants depends on the energy resolution of the EMCAL, momentum resolution of the tracks, and improves as $1/\sqrt{N_e}$, where N_e is the number of electrons per crystal used in calibration.

The detailed GEANT-based description of the BTeV detector has been used to generate simulated electron data. We processed a sample of 10,000 generic B events (generated by Pythia), which contains on the average two non-beauty background interactions per event.
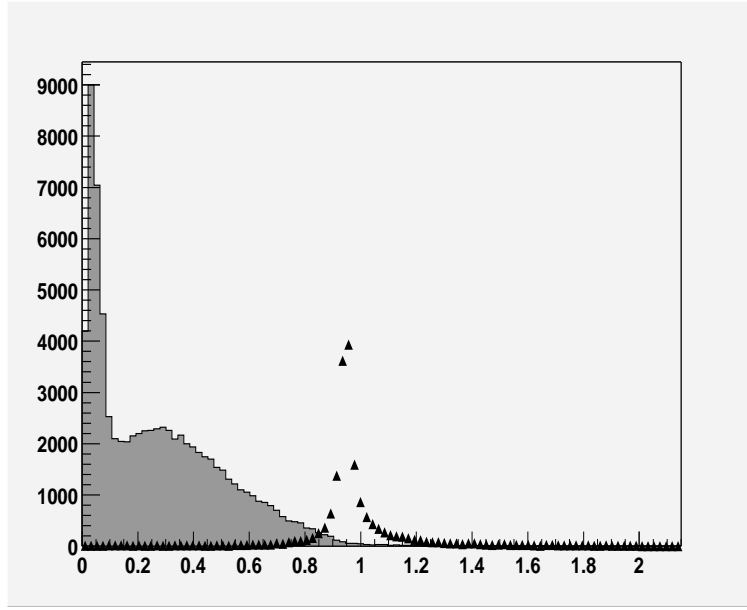
Figure 6.32: Measured ratio E/p for electrons (triangles) and for other charged tracks.

The actual number of these background interactions was fluctuated according to Poisson statistics. When we calculated the digital signal for each crystal, we took into account the energy resolution arising from a photon statistics contribution of 1.6% at 1 GeV and a constant term of 0.5%.

For this study, we selected well-reconstructed charged tracks with momenta greater than 3 GeV that entered the calorimeter fiducial volume. We further required that the projection of each of those tracks at the calorimeter matched with a reconstructed shower within 1 cm.

Figure 6.32 shows the distribution of the ratio of the reconstructed shower energy to the track momentum (E/p) for the accepted tracks. In this figure, the points shows the data for electrons and the histogram is for all other charged tracks. We used energies measured in the 3×3 matrix of crystals centered on the crystal with the highest energy deposit.

As expected, electrons are very well separated from charged hadrons. Only a very small fraction of hadrons will pollute the electron sample. However, there is a non-Gaussian tail on the right-hand side in the E/p distribution for electrons, which indicates that there are contributions in the showers from other overlapping particles, which include radiated photons from the electrons.

We further looked at the isolation variable $E(3 \times 3)/E(7 \times 11)$, the ratio of the energy deposition in the 3×3 matrix of crystals to the energy deposition in the 7×11 matrix. The outer matrix is larger in y because the magnetic field deflects the electron and often radiated photons tangentially, producing the energy deposit pattern wider in the y-direction. Figure 6.33 shows the distribution of the isolation variable for electrons (triangles) and for other charged tracks. We required the isolation variable to be in the range $0.92 < E(3 \times 3)/E(7 \times 11) < 1$.
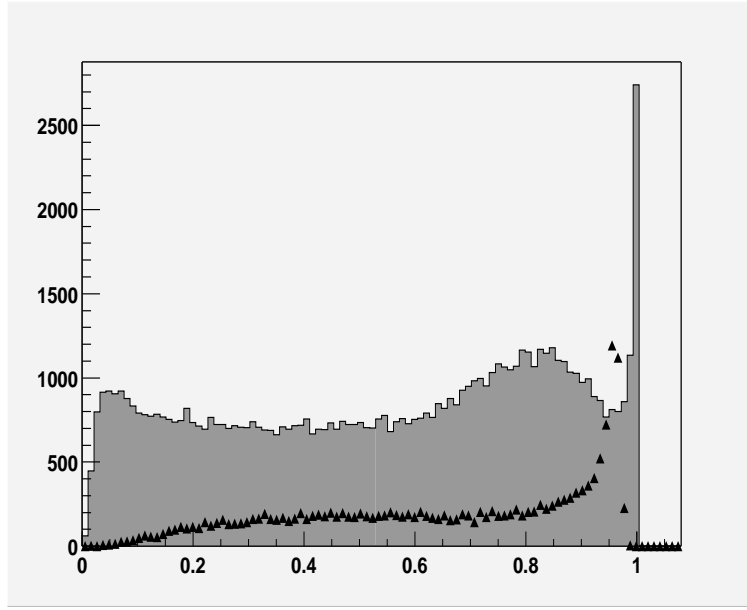
Figure 6.33: Measured ratio E(3x3)/E(7x11) for electrons (triangles) and for other charged tracks.

Figure 6.34 shows the E/p distribution for isolated electrons, those which passed the $E(3 \times 3)/E(7 \times 11)$ cut. From a Gaussian fit, we obtain $\sigma(E/p) \simeq 1.9\%$. The statistical precision of the E/p peak position is given by $\sigma(E/p)/\sqrt{N_e}$, where N_e is the number of electrons available for calibration. Thus, in order to achieve 0.2% calibration precision, we will need to collect ~ 100 e's per crystal.

Our electron signal can be further improved in two ways. First of all we could use a 5x5 crystal matrix here to obtain better resolution and secondly we can identify electrons in the RICH below 22 GeV. These were not done in this study because we wanted to see how well we could do without these clean up criteria.

There are 3443 entries in the E/p distribution within $\pm 2\sigma$ around the peak in a total of 10,000 Monte Carlo events. This means that there are ~ 0.34 electron/event hitting somewhere in the EMCAL.

However, these electrons are not distributed over the calorimeter uniformly. Figure 6.35 shows the ϕ-distribution of these electrons. The two clear peaks at ± 90 degrees reflect the effect of the magnetic field that sweeps charged particles in the y direction. It follows that the rate of collection of electrons useful for calibration varies by a factor of 20 between the extreme cases even at the same radius. The value of $\sigma(E/p)$, however, does not change from one area to another area of the calorimeter.

More detailed studies of the distributions of electrons over the calorimeter show that we will be collecting the electrons at the following rate:

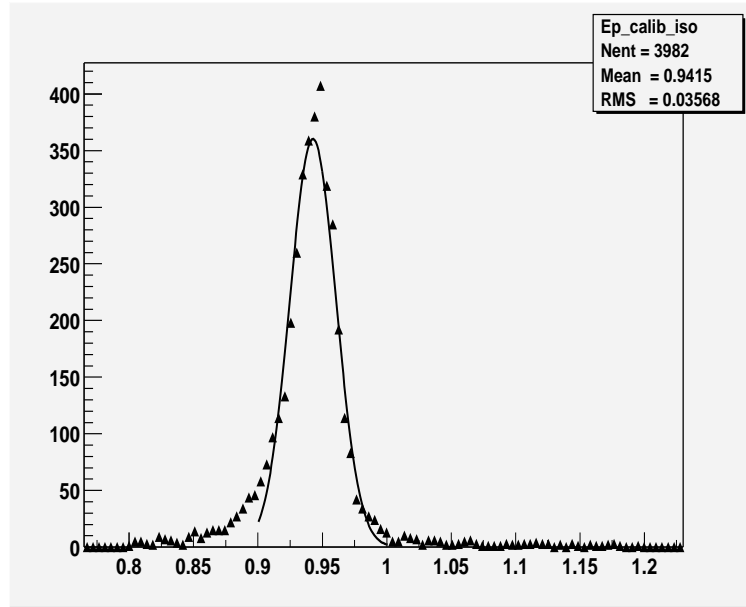- $\sim 8\%$ of crystals will receive $\sim 1.7 \times 10^{-4}$ e's/crystal/event

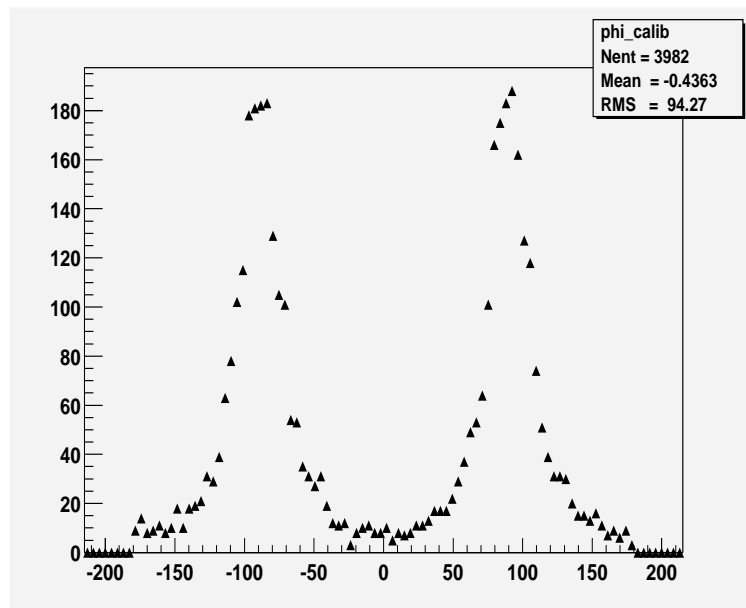Figure 6.34: Measured E/p distribution for isolated electrons

Figure 6.35: ϕ-distribution for isolated electrons

6-47

- $\sim 14\%$ of crystals will receive $\sim 1.0 \times 10^{-4}$ e's/crystal/event

- $\sim 11\%$ of crystals will receive $\sim 5.0 \times 10^{-5}$ e's/crystal/event

- $\sim 22\%$ of crystals will receive $\sim 2.0 \times 10^{-5}$ e's/crystal/event

- $\sim 45\%$ of crystals will receive $\leq 1.0 \times 10^{-5}$ e's/crystal/event

The narrow area along the y-axis can be calibrated with electrons almost continuously (every hour), while for the calibration of the least covered 45% of the calorimeter, we will need to collect $(10-15) \times 10^6$ events to obtain about 100 electrons/crystal. This corresponds to several hours of running at nominal luminosity.

To conclude this section, we will be able to calibrate the crystals at least once every several hours, certainly once every day, while some of the highly irradiated parts of the calorimeter could be calibrated every hour.

6.5.2 Light Pulser System

6.5.2.1 Overview

The light pulser system is used to monitor changes in the light output from the PWO crystals, and also gain changes in the PMTs. Because the PMT gain change affects the signal from the light pulser and scintillation signal in the same way, the fractional changes in these two signals will be exactly the same. In other words, the ratio in the fractional signal changes is expected to be 1. *i.e.*

$$R = (\Delta_{\text{Scint}}/S_{\text{Scint}})/(\Delta_{\text{LP}}/S_{\text{LP}}) = 1, \tag{6.5}$$

where S and Δ represent the signal and its variation, and subscripts "Scint" and "LP" represent scintillation signal and light pulse signal. This means that correcting our scintillation light signal for the PMT gain changes using the monitoring system is straightforward. However, different PMTs have quite different $\Delta_{\text{Scint}}/S_{\text{Scint}}$ for similar running conditions, as is clearly shown in Fig 6.36.

This is not the case for the changes in the light produced in the crystals. When the transparency of the PWO crystal deteriorates due to radiation, which is believed to be the only radiation damage mechanism in the PWO crystal, it reduces both the LED signal and particle signal. Since there are different optical paths taken by the injected monitoring light and the scintillation light, the fractional losses of the two sources of light are somewhat different. However, the relation between the two losses is more-or-less proportional as long as the absorption length is much longer than the crystal length. This suggests that the above ratio will still be a useful quantity but will not be 1. In order to find $\Delta_{\text{Scint}}/S_{\text{Scint}}$ from $\Delta_{\text{LP}}/S_{\text{LP}}$, we need to know the value of R for each crystal. We will discuss how we plan to obtain the R values in section 6.5.2.5 below.
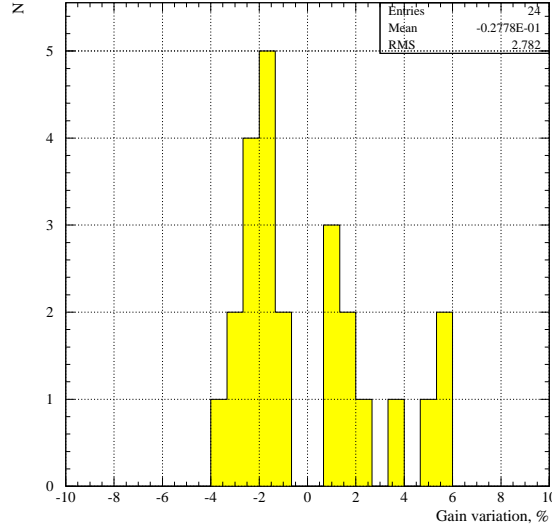
Figure 6.36: Distribution of gain variations of 6-stage Hamamatsu phototubes in the test-beam study.

Because of these differences in the values of R and variations in contributions to changes from PMT gain variations and crystal light outputs, we have decided that it is important to monitor these two changes separately.

To monitor a change in the crystal light output, we will use a blue light pulser of 470 nm wavelength close to the 430-nm emission peak of the PWO crystal. Since the signals from these blue light pulses are detected by PMTs, what we measure is the change in the product of the PMT gain and light output. In other words, the fractional change we measure is the sum of the fractional changes in the PMT gain and the crystal output. Correcting for the PMT gain change obtained in the method described below, we can separate the light output change.

If we could send calibration light pulses to PMTs directly, it would be easy to measure PMT gain changes. However, we cannot do this because each of the crystals covers the entire detection surface of the mating PMT. We chose the color of the light pulses for this task to be red, since its transmission in the crystal does not change due to radiation.

In the test beam studies, the separation of these two sources of signal variations has been crucial so that we could study the changes in the crystal properties alone. Our experience with a blue-red light pulser system at the test beam facility is described in section 6.5.2.2. This section also gives the results of our studies on the values of R for different crystals for electron and pion irradiation.

In section 6.5.2.3, we discuss our current design of the pre-production light pulser and performance results.

6.5.2.2 Experience at Test Beam

A LED-based light pulser system with four LEDs of different wavelengths was made for the test beam studies at Protvino to monitor gain variations of the PMTs and transmission variations of the PWO crystals. The LEDs emit at red (660 nm), yellow (580 nm), green (530 nm), and blue (470 nm) wavelengths. For the actual analysis of data, the red and the blue LEDs were most useful.

Between two accelerator spills, 10 light pulses of one color were sent to the crystals. Then in the following interval, light pulses of another color were injected in the crystals. This way, four spills were needed to collect data for all four colors. The light from all the LEDs were fed into the same set of optical fibers and they delivered the light to individual crystals. (*i.e.* there was only one fiber going to each crystal instead of having one fiber for each color LED.

In the test beam set up, the LED light was injected at the front end of the crystals. So the typical path length of LED light in the crystal approximately equals the length of the crystal. Since the light comes out of the optical fiber with a characteristic full angle spread of 25°, and this angle is reduced to 11° as the light enters the crystal from air, the path length of light in the crystal should be increased by $1/\cos 11°$. As for the scintillation light from incident particles, half of the light travels directly to the PMT while the other half will travels towards the front of the crystal and gets reflected before it is detected by the PMT. Averaging between these two cases, the average path length of scintillation light to the PMT also equals the crystal length to the 0-th approximation. In order to estimate the 1st order correction, we need to know how much the light zigzags on its way to the PMT. The maximum angle that the light makes with respect to the crystal axis is determined by what angle the light is reflected by the side surfaces due to the total internal reflection, which is about 64°. This leads to many more zigzag paths than the paths for LED light. Taking into account that the scintillation light is emitted isotropically, the average $< 1/\cos \theta >$ factor arising from the zigzag paths is about 1.4.

The LED system monitors the transparency of the crystal at a specific wavelength (in our case, 470 nm was chosen partially due to the availability of blue LEDs) and thus does not sample the entire spectrum of scintillation light. The radiation damage effect is less severe at 470 nm than at 430 nm, the center of the PWO scintillation emission peak. From these considerations, we expect that the ratio, R, of the light loss factors for the LED signal and the particle signal is about $1/1.4 = 0.7$ to $1/1.6 = 0.6$.

One of our goals in the test beam studies of the calibration system is to measure this ratio, R, experimentally, and how it varies from crystal to crystal. Naively, since this ratio only depends on the geometrical lengths of light paths for the LED and scintillation light, it should not vary from one crystal to the next. If there are variations in the shape of the absorption as a function of wavelength among crystals, the ratio, R, may vary among crystals. In addition, since the crystals will not be polished to optical flatness, actual reflections of light by the side surfaces do not follow the simple law of geometrical light reflection. This may also lead to variations of the ratio, R, among crystals. Thus we feel that it is very important to measure the variation of R values experimentally.

Since it is not practical to measure this ratio for all production crystals at a test beam
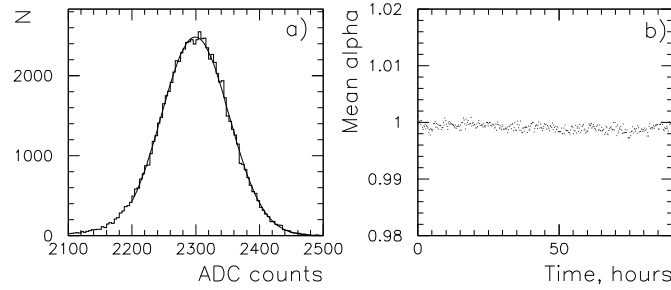
Figure 6.37: (a) α energy spectrum accumulated over 1.5 hours. (b) α spectrum peak position as a function of time over 85 hours. Each point corresponds to a 15-minute measurement duration.

facility (it would take too much time), we need to know if the variation, if there is one, is small enough so that we will not spoil the resolution even if we assume and use an average value of the ratio for all crystals.

6.5.2.3 Monitoring Systems for the Light Pulser System and Stability of Light Pulser

We built two monitoring systems to check the stability of the magnitude of the light pulses. (*i.e.* monitoring systems of the monitoring system.) One was based on a PIN photodiode, which is considered very stable even when the temperature varies. According to some literature, the temperature variation of PIN photodiodes is less than 0.01%/°C. However, since we needed an amplifier to detect the PIN photodiode signal, the amplifier gain needed to be stabilized by housing it in the crystal box where the temperature was stable to $\pm$ 0.1 C.

The second system used a PMT, scintillation crystal and radioactive source. The PMT (Hamamatsu R5900) monitored the LED pulser while the PMT was monitored using the stable scintillation light produced when a $YAlO_3 : Ce$ crystal was irradiated with an ^{238}Pu alpha source (YAP) [13]. The α energy spectrum measured by the PMT and the peak position of this spectrum as a function of time is presented in Fig. 6.37. The width of the peak is 2.3% r.m.s. as determined by a fit to a Gaussian. The peak position was stable over 85 hours to better than 0.2%.

The measured variations (drifts) of the magnitudes of light pulses (averaged over 120 pulses) over different time periods were measured, for the periods of test beam studies. They were:

- 0.1 to 0.2% over a day;

- 0.5% over a week;

- 1% over a few months.

Temperature variations were the main cause for the variations in the sizes of pulse. When corrections based on the temperature were made in the pulse-height analysis, the long term variation significantly decreased to 0.4% over a few months and down to 0.3 % over a week. No LED ageing effects were observed after 3000 hours of operation.

The stability of this system was better than we needed to monitor the gain variations of the PMTs and the transparency variations of the crystals over the relevant time periods. For example, we were able to track the crystal transparency change with an accuracy of better than 1% over a week when we measured how much radiation damage the crystals suffered. Additionally, we were able to track the crystal transparency change with an accuracy of better than 1% over a few months when we measured the recovery process of the radiation-damaged crystals. Finally, it made it possible for us to track the PMT gain variations over a day well enough so that it did not contribute appreciably to energy resolution measurements. This last accomplishment implies that we already have a good enough system for BTeV except that we need to have a much larger system, and temperature stabilization must be considered.

6.5.2.4 PMT gain monitoring

A similar study was done when the beam intensity changed in the later test beam runs where we used a red LED light pulser system to monitor the PMT gains.

When we installed the red LED in the monitoring system, we were able to correct our data for the PMT gain changes. The blue LED signal amplitude, which measures the changes in the crystal transparencies, are shown in Fig. 6.38 as a function of time over 85 hours. The middle plot shows the raw signal from the blue LED, which shows decreases in the signal when the electron beam intensity went to zero. The beam intensity is shown in the top plot of this Figure. When these data are corrected for the PMT gain variation using the red LED data, we found much smoother results, which are shown in the bottom plot.

In our analyses of the electron beam data described in the previous sections, we corrected the signals from electrons and blue LED, using the red LED data.

6.5.2.5 Crystals Light Output Monitoring

As it was described in the section 6.3.5, crystals behave in a similar way in the radiation environments of different nature; clear correlations between electron and LED signal changes was observed. The dedicated study has been carried out to confirm that these correlations are not dependent on the type of irradiation using a particular optical monitoring scheme. To be more specific, the same crystals were calibrated with a low intensity electron beam first, then they were exposed to the highly intense electron radiation. Crystals irradiation continued with pion beam. Both electron and pion irradiations alternated with calibration runs using low intensity electron beam. Changes in the crystals transparency were monitored continuously with the use of the LED monitoring system. Linear fit of the distributions of the relative blue LED signal change vs electron signal change was done for both electron and pion irradiations. Coefficients of the linear fit are presented in Fig. 6.39
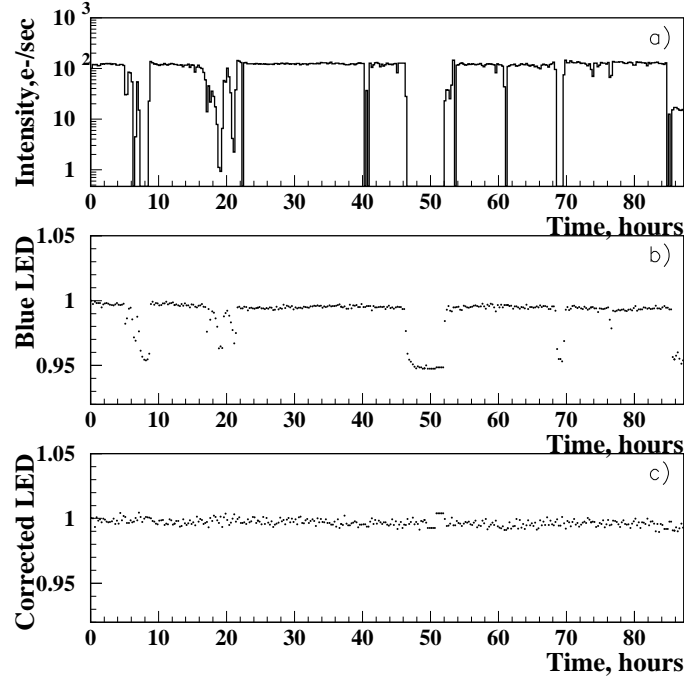
Figure 6.38: (a) Electron beam intensity in the Shanghai crystal S22 as a function of time. Blue LED behavior for this crystal (b) before and (c) after PMT gain change correction using the red LED data.

As it was expected, on average the measured coeffitcients are not different and are in a good agreement with the calculations for the current optical scheme. The fact that the linear approximation works well significantly simplifies the procedure of the EMCAL inter-calibration that will be performed using an LED-based light monitoring system over the time intervals between two consequent in situ calibrations.

6.5.3   Light Monitoring System for BTeV Calorimeter

The light monitoring system, shown schematically in Figure 6.40, is designed to inject light pulses into each PWO crystal in order to measure optical transmission near the scintillation spectrum peak (430 nm). The red light pulses are used to monitor PMT gain stability. The system includes both blue and red LEDs, their driver circuits, and optical fibers to deliver light pulses to each of the PWO crystals.

We plan to use very powerful LEDs, assisted by a reflector and a light mixer so that each light pulsing system produces enough light for ~2700 crystals, each receiving light pulses equivalent to scintillation light from 20 GeV photons. The distribution of light among the 2700 fibers should be very uniform. This is accomplished by designing a good light mixer

Pion

Electron

Entries	32
Mean	0.6643
RMS	0.9228E-01

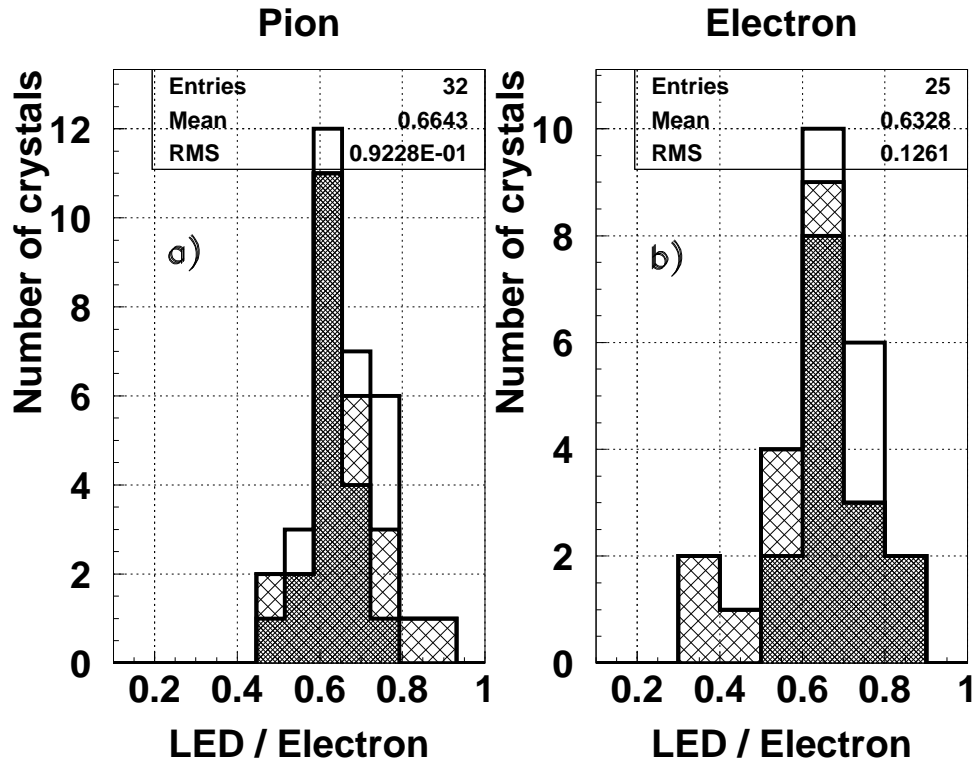| Entries	25
Mean	0.6328
RMS	0.1261

a)

b)

Figure 6.39: Linear fit coefficients calculated from the correlation plots of the blue LED vs. electron signal relative changes under pion (a) and electron (b) crystal irradiation.
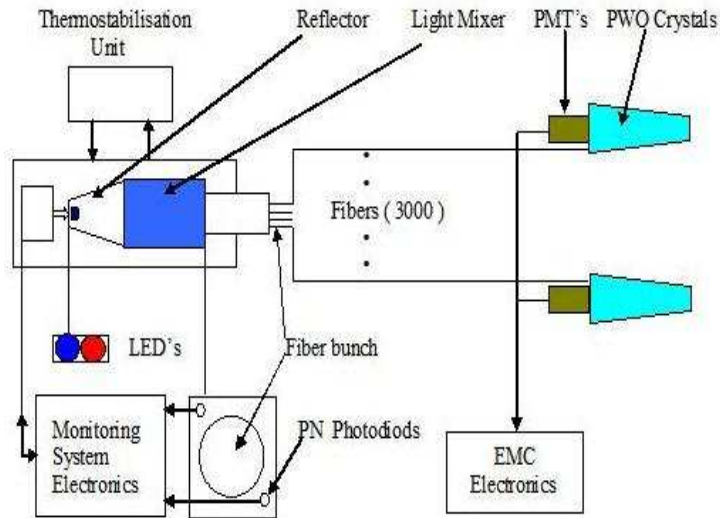
Figure 6.40: Diagram of one quarter of a light monitoring system for the BTeV calorimeter

6-54

which will distribute light uniformly across an area of 38×38 mm^2. Each bunch of fibers (of about 3,000 fibers, of which 400 are spares) and two referenced PIN silicon photodiodes will be contained in this area. Four such light pulsers will serve the whole BTeV calorimeter.

The time dependence of pulse heights from the pulser is monitored by the two reference PIN photodiodes. One of the four pulser systems will be activated at any given time to limit the power requirements of the light source, the size of data transfers, as well as high and low voltages current demands.

The system is designed to continuously monitor the calorimeter in two ways:

- Continuous in-fill monitoring during 2.617 μs gaps in the Tevatron beam structure (beam abort gaps). Less than 10% of these gaps should be sufficient to collect enough data for this purpose.

- Stand-alone monitoring runs between Tevatron fills to follow recoveries of the PWO crystals.

The principal goal of the system is to monitor short-term variation in the PMT gains and the light transmission of the crystals. The system will also be used to check out the entire crystal-readout chain during the assembly of the calorimeter. It will also permit a rapid survey of the full BTeV calorimeter during the installation or after long shutdowns. Furthermore, the light monitoring system can be used to measure the response linearity of the PWO crystal's photodetector and its readout chain. This should complement measurements with electronic charge injection at the preamplifier level which does not test the photodetector.

Some results obtained with a prototype system are presented in section 6.5.3.3.

A picture of the whole prototype system is presented in Figure 6.41. Four such boxes will be mounted on the EMCAL mechanical structure. Each of them will feed ~2,500 PWO crystals by a monitoring light through the fibers. A led driver is presented in Figure 6.42.

6.5.3.1   Monitoring system components

The monitoring system will be located directly at the outer radius of the calorimeter support structure and an optical-fiber light distribution system connects the pulser to the crystals. Since the light pulser is located in a low radiation zone, its components and electronics are not required to be radiation hard. In contrast, many fibers are routed through a high radiation zone and they must be made of radiation-hard materials.

The characteristics of the LEDs we plan to use in the BTeV calorimeter monitoring system are given in Table 6.6:

Besides the exceptional luminous fluxes, we find that two additional features of the Luxeon technology are very important for our monitoring system: very long operating life (up to 100,000 hours in DC mode); and small temperature dependence of the light output (0.1%/C). The producer is Lumileds Lighting, USA. The reflector which was made at IHEP has a trapezoid shape and is made of aluminum plated Mylar or Tyvek.

The optical fibers we plan to use are produced by Polymicro Technologies, USA. Their properties are:

Figure 6.41: View of the prototype monitoring system. Inside the box there is a led driver, blue and red LEDs, a light mixer, a temperature stabilization system, and a referenced PIN-diode system. In use we have a fiber bunch coming out the far side of the box instead of the cables which are pictured; the cables are for tests only and will not go to the BTeV calorimeter. The size of the box is 370 mm x 70 mm x 60 mm.

Table 6.6: Properties of LEDs

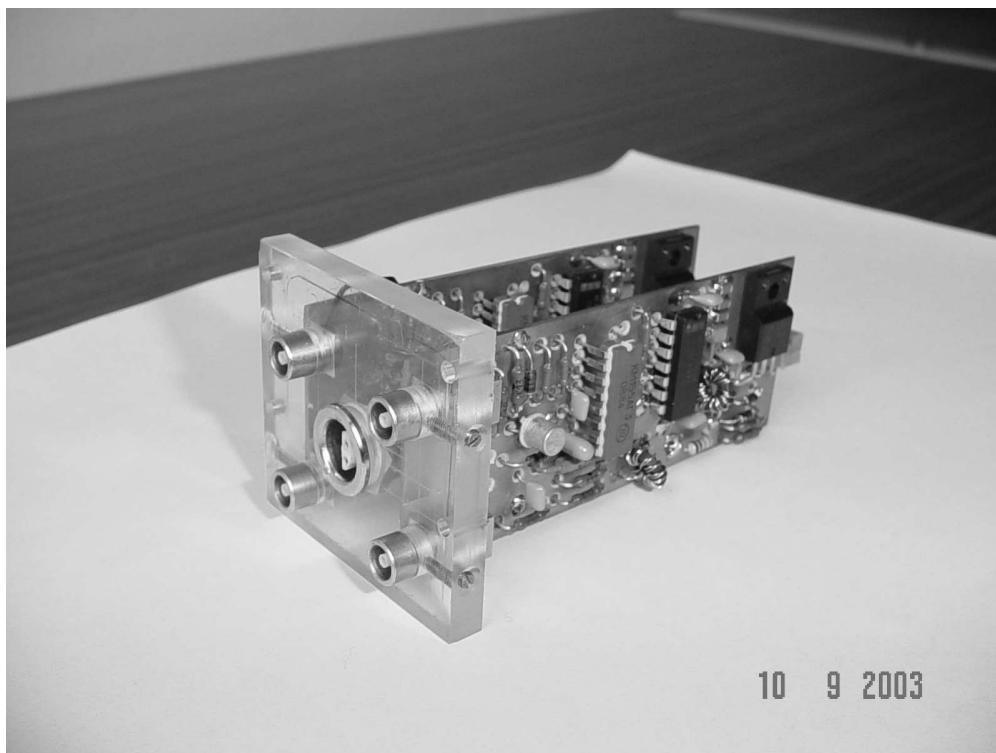| Property	blue (royal blue) LED	red LED
Brand	Luxeon 5-W emitter	Luxeon 1-W emitter
Typical Luminous flux	30 lm (@700 mA)	45 lm (@350 mA)
Radiation Pattern	Lambertian	Lambertian
Viewing Angle	150 degrees	140 degrees
Size of Light Emission Surface	5×5 mm^2	1.5×1.5 mm^2
Peak Wavelength	470 nm (455 nm)	627 nm
Spectral Half-width	25 nm (20 nm)	20 nm
Average Forward Current	700 mA	350 mA

Figure 6.42: LED driver of the Prototype of the monitoring system. It will be inside the box (see the previous Figure) near the side opposite to the one with a bunch of fibers.

- Silica / Silica optical fiber

- High - OH Core

- Aluminum Buffer

- Core Diameter 270 micron

- Outer Diameter 400 micron

- Numerical Aperture 0.22

- Full Acceptance Cone 25.4 Degrees

This fiber has very good radiation hardness. According to the tests made by the CMS ECAL group, this fiber has shown no signal degradation under gamma irradiation with an absorbed dose of up to 12 Mrad.

6.5.3.2   Reference PIN silicon photodiodes

An essential element of the light monitoring system is a stable reference photodetector with good sensitivity at short wavelengths. PIN silicon photodiodes with a sensitive area about
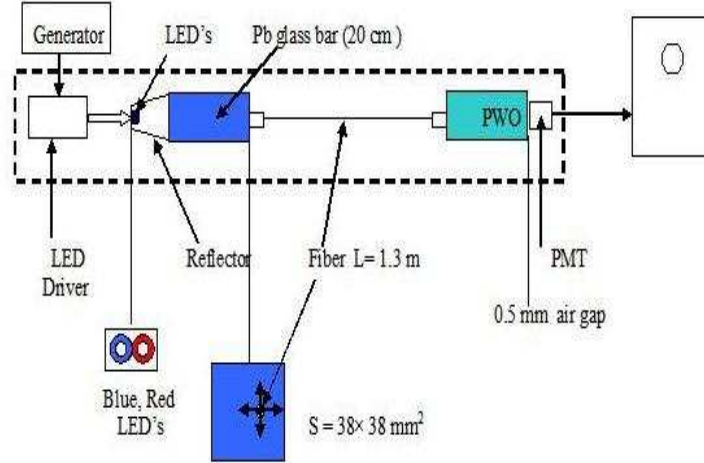
Figure 6.43: Schematic view of the light pulser prototype

6 mm^2 are well suited to this task. In particular, such low leakage currents are achieved with PIN diodes, due to their very narrow depletion zone resulting from heavy (p and n) doping, which is less sensitive to the type inversion than typical PIN diodes. The rather large sensitive area of this photodiode allows us to work without preamplifiers and improve the stability of the reference system itself. A PIN silicon photodiode S1226-5BQ (Hamamatsu) was used in our test measurements. It has an active area of 2.4×2.4 mm^2 and a dark current less than 50 pA (at 5V reverse-bias voltage).

6.5.3.3   Tests of the light pulser prototype

A schematic view of the light pulser prototype is shown in Figure 6.43. The light distribution uniformity was measured with a single fiber scanner. All the measurements were made with a scope and a manual scan with a step size of 2 mm. The scan area was 34×34 mm^2. The result are shown in Figure 6.44 The FWHM of this pulse height distribution is 2%, and the full width is 8%. The energy equivalent is 20 GeV for the whole scan area. The average forward current in the tests was 20 mA. The maximum forward current is 700 mA. So we have a large safety factor for the amount of light. This light pulser can illuminate more than 3000 fibers.

The short-term stability of light uniformity over the area of 34×34 mm^2 for a day has been measured to be 0.05% and a long-term stability was 0.1% over 20 days. In spite of these encouraging results, thermostabilisation of the light pulser by means of the Peltier cell is foreseen in the design of the whole system.
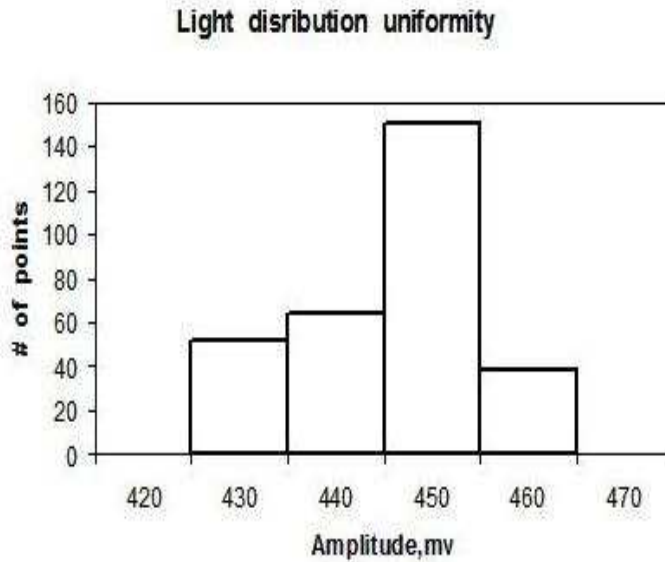
Figure 6.44: Distribution of pulse heights (in mv) measured over an area of 34x34 mm^2 in 2 mm steps.

6.6 Mechanical Structure

The mechanical support design for the BTeV calorimeter is dictated by the need to support many dense crystals with minimum amount of support materials in front and between each crystal. To achieve the physics goals of BTeV, the mechanical support system of the calorimeter has to meet the following requirements:

- The calorimeter mechanical support structure should have material with as low a radiation length as practical in front of and between the crystals so that the calorimeter energy resolution is not compromised.

- The design must take into account that the operating temperature of the detector inside will likely be between 15° and 20° C. Even though the temperature at different locations inside the calorimeter may vary a few degrees C, the temperature variations over a day at any locations must be maintained to ±0.1° C (rms) and over a month, to ±1° C (rms) when the ambient temperature is maintained to ±1° C (rms).

- Thermal stress must be considered so that the mechanical stability of the system will not be affected.

- The support structure should allow us to replace PMTs or crystals.

- The support structure should be retractable to allow service of the silicon strip detectors at station 7.

6-59

- The support structure should allow partial or complete assembly of crystals in the assembly hall and transportation to the collision hall.

- The structure should also allow partial assembly in the collision hall.

- The support structure should have provisions to support electronic crates located at the periphery and to support and guide cables from PMT bases to electronic crates.

- The calorimeter holder needs to be gas tight so we can flow dry air or nitrogen in order to avoid humidity. The humidity level should be kept below 1%.

- We must be able to align the calorimeter system during the assembly stages relative to the pixel detector using suitable alignment marks. The requirement on the accuracy of the calorimeter location is 5 mm. This should be sufficient since we will have to find the position of the calorimeter relative to the pixel detector using data to determine accurate positions.

- Monitoring of the location changes should be known to an accuracy of 1 mm. Relative positions of crystals should be known within 1 mm from the nominal position of each crystal. Changes in the crystal positions relative to the "center" should be stable to 0.1 mm over a day and 1 mm over a month.

Our proposal had assumed that we will use some variant of the CMS endcap structure to support the BTeV PWO crystals. However, the carbon-fiber based cell structures that CMS will use are fairly labor intensive, and even if we produce them in Russia where this type of labor is much cheaper than in the Western Hemisphere, they would still be too expensive. Our IHEP colleagues had a different idea using aluminum strips to form these cells, similar to what was done with the CLEO CsI calorimeter. Since then, FNAL engineers took over the idea and carried out much of the engineering design work.

The overall structure in the front view is shown in Fig. 6.45. The vertical lines (label 1 in the figure) represent vertical strips which are 0.3 mm thick and 250 mm wide. The horizontal lines (position 2) represent horizontal strips of the same thickness and 40 mm in width. They run through holes in the vertical strips with interlocking notches in two places for each row of crystals. One supports the front and the other supports the back parts of the crystals. Other labeled features in this figure are as follows : 3 - top beam, 4 - lower support, 5 - Hillman roller, 6 - trolley, 18 - balance support, 19 - electronics box.

In order to get a better sense of how these strips can be assembled, and also investigate the cost of production of such a structure, we have built a prototype model. It was successfully built using parts fabricated by a commercial shop. Fig. 6.46 shows the front view of the prototype in whole and detail, which has five vertical strips hanging from the top of the frame, and three sets of horizontal strips running from one side to the other. The top set of horizontal strips are inclined at the same angles as strips near the top of the BTeV calorimeter. The middle and the bottom sets emulate those strips near the mid-height and the bottom of the calorimeter.
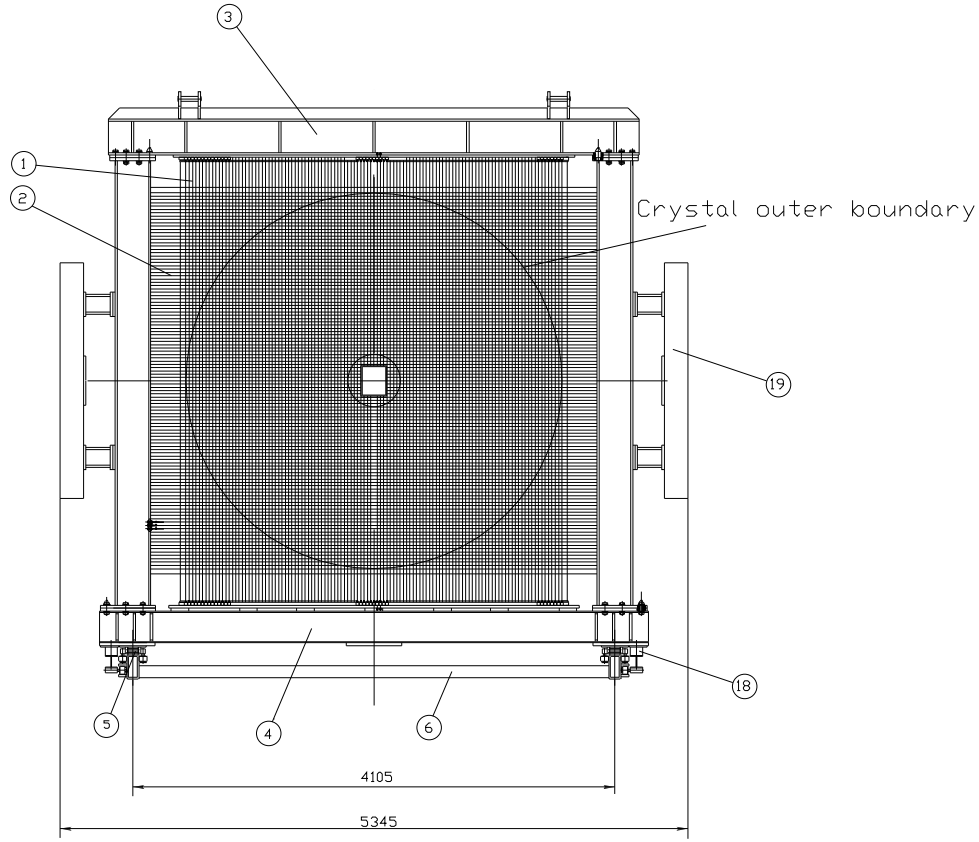
Figure 6.45: Mechanical Structure

6.6.1 Cooling and Humidity Control System

Since the light output depends strongly on the temperature (-2.3%/°C, see section 6.3.4.1), the temperature of the crystals must be stable to 0.1 C(rms). The maximum temperature deviation, once equilibrium is reached, shall not exceed 0.1 C on any temperature sensor near the crystals. The time dependence of the temperature at each monitor point shall be stable to 0.1° C over a day and 1° C over a month. When there is an access to the detector and temperatures inside the detector change, after they settle to plateau values, the temperatures should be back to the pre-access time within $\pm 1°$ C (rms).

The calorimeter is expected to operate at temperatures from 15° to 20° C. Even though we would detect more light from PWO crystals at lower temperatures, we decided that this gain does not warrant the engineering complications, such as dew formation, of keeping the operating temperature below 15° C.

The current in the PMT bases and PMT's dominates the internal heat load. However, this will most likely be overwhelmed by heat flow from outside. The internal heat load comes from the power dissipation of 30 mW per crystal in PMTs near the beam pipe (in the worst

Figure 6.46: Prototype Mechanical Structure

case). For the outer crystals, this drops to 30 μW. So the performance of the cooling system has to be able to deal with the heat flow through the insulation around the detector.

We studied temperature stabilization schemes. Since the heat dissipation by the voltage dividers and the currents in the PMTs is minimal (20 W), our major concern was the heat flow from the ambient $(25\pm1)^\circ$ C air to inside the temperature controlled environment.

We modeled the thermal properties of major components of the calorimeter, and found that when we surround the calorimeter with two 0.375 inch thick Rohacell boards and temperature-regulated air flows in 0.75 inch of space between them, we can maintain the inside temperature at $(15\pm0.1)^\circ$ C [14].

Humidity must be low enough for stable PMT HV operation, thus the system will be sealed and dry air or nitrogen gas will be flowed through, in order to keep the relative humidity below 1%.

6.7 Detector Assembly, Installation and Integration

The calorimeter consists of PWO crystal-PMT assemblies (glued together) and PMT bases which will be inserted into a mechanical support structure. The mechanical structure is made of a strong frame to support the entire weight of the device, and interlocking vertical and horizontal strips which form cells, where individual crystals will be inserted. The mechanical structure will be surrounded by insulating layers to help reduce the thermal load on the temperature stabilizing system.

In addition, electronics racks, which hold Front-End Boards (FEB), will be mounted near or on the mechanical structure. Cable trays will also be installed on the support structure for signal and HV cables as well as optical fibers.

Optical fibers that will be used to monitor and calibrate the crystal transparencies must be attached to each crystal. They will be useful to test the functionality of each crystal in the testing phase.

The support system will be assembled either outside the C0 Hall or in the assembly area of the C0 Hall. Crystal-PMT assemblies will be inserted into the support structure as much as possible prior to moving it to the collision hall, though with the current schedule, we will not have much time to do so.

Most of the crystal-PMT assemblies will be installed in the collision hall, with some number of the assemblies being installed each time we have access to the hall. Testing of the installed crystal-PMT combination will be done on a daily basis using a light pulser to assure all crystals are functional.

When FEBs become available, we will connect the PMT outputs to FEBs and test the whole sequence up to the FEB's using a temporary DAQ system, which will read out a section of the calorimeter. A clock will be required for multiple crates but we will supply this if it is not available from the PC-based DAQ system.

When the BTeV DAQ is available, the entire connections will be made to it and the final testing will be done with whatever triggers are available at that time.

When particle-based triggers become usable, we will start checking for mis-cabling and working on alignments.

6.7.1   Testing Prior to Moving to C0

The elements moved to C0 should be tested sufficiently to ensure their functioning. C0 is not intended to be a general testing laboratory. However, if some items are too large to test anywhere else, they can be tested at C0. Crystals are glued to PMT's and tested for functionality before they are inserted to the support structure. Separately, signal and HV cables as well as optical fibers for calibration will also be tested. FEBs will be tested individually and in the crates before they are brought into C0 for connections to PMT's. The mechanical support system will be tested against the specification including mechanical tolerances and integrity.

6.7.2   Transportation of Elements to C0

Assuming that the mechanical structure is assembled outside the C0 hall, it will be brought to C0 by a truck. The entrance door to the C0 building is too small for the structure to pass either horizontally or vertically. A large fork lift will be required to unload the structure from the truck and tilt it to 45° for rolling through the C0 building door.

The partially crystal-filled structure will be pushed (pulled) on its wheels to the collision hall. It will be moved using a transportation cart. Standard rigging equipment along with floor/wall anchors used for the magnets will be used.

Crystal-PMT assemblies will be brought to C0 in a box. A simple lifting device (200 kg) will be used to handle this box safely.

6.8   Detector Performance

6.8.1   ECAL Simulation

The BTeV ECAL geometry has been implemented as a part of BTeVGeant, our current simulation packaged based on GEANT3.21. A detailed description of BTeVGeant is given in the Proposal.

The current version of BTeVGeant incorporates a more realistic ECAL geometry description compared to the simplified version used at the time of the Proposal, since there has been progress in the mechanical design.

Currently, the BTeV detector has one electromagnetic calorimeter, at positive Z arm. It consists of more than 10,000 Lead Tungstate ($PbWO_4$) crystals. The crystals, all of the same size, are tapered; the transverse dimensions are square, 2.72x2.72 cm^2 at the front and 2.8x2.8 cm^2 at the back, with a length of 22 cm. Each crystal is surrounded by air gap of 0.02 mm on each side, to account for clearance. In between there is 0.75 mm of Aluminum for the support structure. The crystals are installed to point almost at the I.R., i.e. to point at x = -10 cm, y= -10 cm from the I.R., to minimize the effect of gaps, but give the benefits of a projective geometry. The outer boundary of the ECAL is close to a 160 cm radius circle. There is an inner square hole, $\pm$ 10.88 cm in x and y, in the ECAL to accommodate the beam. The ECAL is positioned at 750 cm from the center of the interaction region.

GEANT3 permits users to control the thresholds and cutoffs of the many physics processes that it simulates. Low thresholds give more realistic and detailed simulations but can require a large amount of computer time. This, in turn, can make it difficult to simulate large enough samples of events to make precise statements about efficiency and background rejection. After investigating several combinations of energies below which the tracking of electrons and photons is stopped, we selected 1 MeV threshold on both. A detailed description of the cutoffs selection study is done in the Proposal (pages 158-167).

The ECAL response is simulated in a form of "hits", where a hit is a sum of the energy deposition in a $PbWO_4$ crystal by one or more electromagnetic or hadronic showers. The energy stored in the hit is the true energy which would be measured by a perfect device. The hits are serialized and written to the output stream, along with geometry information in the BTeV specific format, for further reconstruction and analysis.

Effects such as light collection efficiency, readout specifications and imperfections are applied in a parametric way at the reconstruction and/or analysis time. Therefore these can be varied without CPU-expensive rerunning of BTeVGeant. This approach has been used a number of projects, in particular by CMS, and has been shown to be reliable. The

data structure for ECAL hits may also optionally store information about which particles or showers contributed to the energy sum in each crystal, should a user request.

6.8.2 Photon and π^0's Reconstruction Procedure

In this section we will describe shower energy and incident position reconstruction, unfolding of overlapping electromagnetic showers, rejection of contributions from charged hadrons, and photon and π^0 reconstruction efficiencies.

The light generated in each crystal by electromagnetic showers or other charged particles is detected and converted into a digitized signal that is proportional to the number of photons incident on the photocathode. After a calibration step these numbers represent the total amount of energy deposited in each crystal for each event. From the array of energies in the ECAL, we extract the following information:

- Shower information that includes a total energy and a position measurement.

- Matching information that connects charged particle tracks and showers.

6.8.2.1 Shower Reconstruction Package

Our shower reconstruction tool, the cluster finder algorithm, is designed to identify specific patterns in the calorimeter hit data. Much of the key ideas were borrowed from reconstruction packages perfected by the Crystal Ball and CLEO crystal calorimeter groups. The two defined patterns are:

- Cluster - a region of crystals with connected topology.

- Bump - a local maximum in the energy response within a cluster.

The first step in the procedure is to create clusters. A cluster is started by a single crystal with energy deposit higher than a tunable threshold called "triggering seed" (no relation to actual BTeV triggering algorithms!) and represents all connected crystals with energy deposit higher than readout related threshold called "visible hit." Currently we use 40 MeV for the "triggering seeds" and 1 MeV for the "visible hits." The starting crystals are selected from the list of crystals with energy deposit higher than the "triggering seed" threshold; the crystals in the list are also sorted by energy.

The shape of a cluster can vary, since it only requires crystals to be neighbors when added to the same cluster. However, a crystal can only be part of one cluster.

The next step is to find bumps in the clusters. A bump is centered around a crystal in a cluster that has the maximum energy deposit into it compared to its adjacent crystals, and thus represents a local maximum. It has a fixed shape made of rings of neighboring crystals. Crystals may belong to one or more bumps. They only need to have energy deposit larger than the "visible hit" threshold. If a crystal is a part of more than one bump, a re-weighting

algorithm will partition the energy deposit in that crystal assigning some fraction of it to each bump to which the crystal belongs.

The most important data generated for bumps are total energy, position and shape, and they are recorded along with each bump object. A program using the output of cluster finder can efficiently access those numbers from memory.

The energy algorithm assumes that a bump represents an electromagnetic showers, initiated by a photon or an electron. Due to the shape of shower propagation, most of the energy is contained in the 3x3 array centered on the crystal with maximum signal, with small leakage into further away crystals. The sum of the energy in these crystal is called E9 because it contains contributions from up to 9 crystals. To estimate total energy of a shower, we chose 5x5 array centered on the crystal with maximum signal; this energy sum is called E25.

To calculate the shower position, called center-of-gravity, the algorithm averages on the positions of all the crystals used in the 5x5 array, weighted by energy deposition in each crystal.

Various effects introduce biases into the raw results obtained using this algorithm. There are basic geometric effects and effects due to limitations on the measurements. Here is the list of important corrections:

- Correction for the leakage outside the 5x5 array of crystals and for losses due to thresholds used in the reconstruction procedure; on average, the losses total at about 2%.

- Position bias correction for the center-of-gravity, know as "S-curve correction."

- Correction for the primary vertex position.

- The clustering algorithm is written in C++ and is organized as a single stand-alone library that accepts user and simulation input data, generates the above described bump objects, and gives access to the information stored in them. The described corrections parameters were found using single photons and π^0').

6.8.2.2   Rejection of Contributions from Charged Hadrons

Photon showers candidates selection is based on two criteria:

Shower shape criteria relies on the fact that the transverse profile of a hadronic showers is usually wider than that of an electromagnetic one. The E9/E25 ratio is used as a shower shape criteria to test the hypothesis that the bump represents an electromagnetic shower rather than a hadronic shower. Figure 6.47 illustrates the distribution of this ratio for single photon simulated by GEANT.

Contributions from charged hadrons, as well as from electrons, are further reduced by applying the isolation criteria. Tracks are projected onto ECAL, and for each shower a distance to the nearest footprint of a charged track is calculated, then required not to exceed a certain value. An exact value of the isolation criteria depends on a particular analysis and may vary when studying one B-decay mode or another.
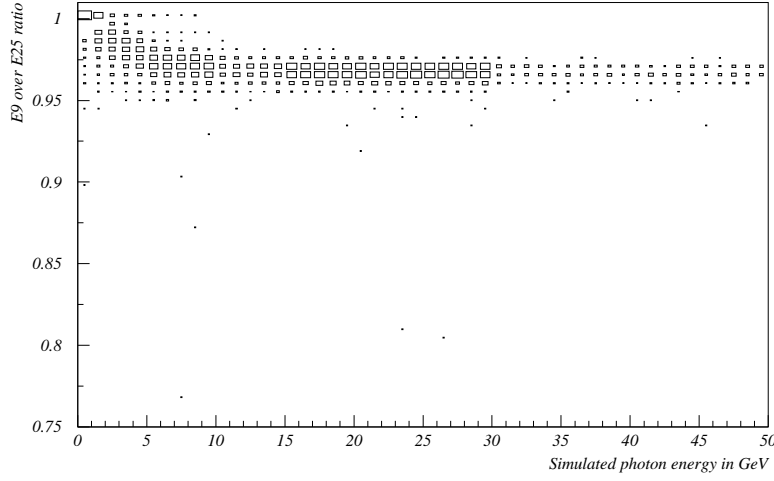
Figure 6.47: Measured ratio of E9 over E25 versus simulated photon energy.

6.8.3   Physics Simulation

Several studies have been done for various physics processes as reported in the proposal update. Here we reproduce one of these studies that we have continued looking at because of its importance. We report on the expected performance of the BTeV detector for the decays $B^0 \rightarrow (\rho\pi)^0 \rightarrow \pi^+\pi^-\pi^0$ to demonstrate the usefulness of the BTeV EMCAL to detect photons. These decays are very important to study as the asymmetries in these decays can be used to measure the so-called the α angle of the CP triangle, which is difficult to obtain with other decays.

Following the paper by Quinn and Snyder [15] and using their notation, the amplitude for the decay $B^0 \rightarrow \rho\pi$ can be written as:

$$
\begin{aligned}
A(B^0 \rightarrow \rho^+\pi^-) &= S_3 = T^\pm + P_1 + P_0 \\
A(B^0 \rightarrow \rho^-\pi^+) &= S_4 = T^\mp - P_1 + P_0 \\
2A(B^0 \rightarrow \rho^0\pi^0) &= S_5 = -T^\pm - T^\mp + T^{+0} + T^{0+} - 2P_0
\end{aligned}
\tag{6.6}
$$

Here the penguin contributions (P_i) are identified by the isospin of the final $\rho\pi$ state to which they contribute. Tree contributions are denoted by T^{ij}, where i and j denote the ρ and π charge, respectively. The amplitude for $B^0 \rightarrow \pi^+\pi^-\pi^0$ can the be written, ignoring non resonant contributions, as:

$$
A(B^0) = f^+ S_3 + f^- S_4 + \frac{f^0}{2} S_5
\tag{6.7}
$$

$$
A(\bar{B}^0) = f^- \overline{S}_3 + f^+ \overline{S}_4 + \frac{f^0}{2} \overline{S}_5
\tag{6.8}
$$

where the Breit-Wigner functions are given by

$$f^{\pm 0}(s) = \frac{\cos(\theta)}{s - m_\rho^2 + i\Pi(s)} \tag{6.9}$$

and running decay width is given by

$$\Pi(s) = \frac{m_\rho^2}{\sqrt{s}} \left(\frac{p(s)}{p(m_\rho^2)} \right)^3 \Gamma_\rho(m_\rho^2), \tag{6.10}$$

where s is the square of the invariant mass of the two pions, and θ is the angle in the ρ rest frame between a decay pion and the line of flight of the bachelor π.

From eq. (6.6) it follows that

$$S_3 + S_4 + S_5 = T^{+0} + T^{0+} \equiv T \tag{6.11}$$

and, similarly,

$$\overline{S}_3 + \overline{S}_4 + \overline{S}_5 = \overline{T}^{+0} + \overline{T}^{0+} \equiv \overline{T} \tag{6.12}$$

The angle between T and $\overline{T}$ is α in the Standard Model with no ambiguities in its determination.

The amplitude M_+ for tagged B^0 (M_- for tagged $\overline{B}^0$) is a function of the position in the Dalitz plot and of the time t.

$$M = \begin{cases} M_+ = e^{-\frac{\Gamma t}{2}} \left[\cos(\frac{\Delta m}{2}t)A(B^0) + i\frac{q}{p}\sin(\frac{\Delta m}{2}t)A(\overline{B}^0) \right] \\ M_- = e^{-\frac{\Gamma t}{2}} \left[\frac{q}{p}\cos(\frac{\Delta m}{2}t)A(\overline{B}^0) + i\sin(\frac{\Delta m}{2}t)A(B^0) \right], \end{cases} \tag{6.13}$$

where Γ is the B decay width and Δm is the mass difference between the heavy and light neutral B mass-eigenstates. The dependence on this quantity arises from the $B^0 - \overline{B}^0$ mixing.

The time evolution of the physical states is shown in Figure 6.48 where we can appreciate the deviation from a pure exponential time distribution.

An example of the variation of the Dalitz plot versus time is illustrated in Figure 6.49, where the events are selected using a rejection algorithm based on $|M|^2$ (see eq. (6.13)).

A maximum likelihood fit is performed on the generated events to determine the amplitudes and phases of eq. (6.6), and consequently α.

The log-likelihood is given by:

$$\ln \mathcal{L} = \sum_i \ln \left(\left| \frac{M_i}{M_{\text{norm}}} \right|^2 \right) \tag{6.14}$$

where M_i is defined by eq. (6.13) and the normalization factor M_{norm} is given by:

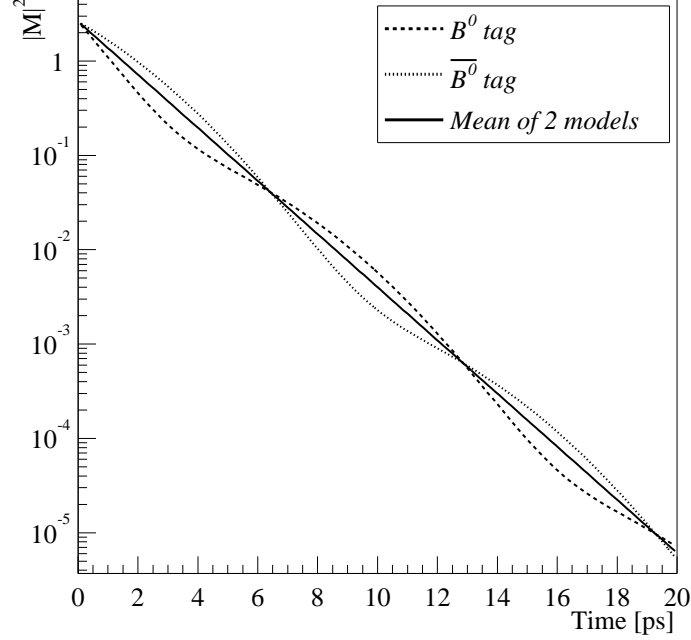$$|M_{\text{norm}}|^2 = \frac{|M_+|^2 + |M_-|^2}{2} \tag{6.15}$$

Figure 6.48: Time evolution of the physical $B^0 - \overline{B}^0$ states.

Excellent resolution in π^0 reconstruction and momentum will reduce the background significantly and to a manageable level, particularly near the edges of the Dalitz phase space where the $\rho\pi$ events lie. In addition, good resolution in the proper time is also crucial to determine the angle α. BTeV, with its PbWO$_4$ crystal calorimeter, will be able to collect and reconstruct a substantial sample of $B \rightarrow \rho\pi$ events.

The reconstruction efficiencies for $B \rightarrow \rho\pi$ and backgrounds were studied using a full GEANT3-based simulation (see ECAL Simulation section), for $\rho^{\pm}\pi^{\mp}$ and $\rho^0\pi^0$, separately. All signal and background samples were generated with a mean of two interactions per crossing. The analysis relies especially on the Kalman filter, the vertex package, and the ECAL reconstruction package.

With the use of the electromagnetic calorimeter, our aim is to find good π^0 candidates. We select candidate "bumps" in the calorimeter using the cluster finder code (see ECAL Reconstruction section). Photon candidates are required to have minimum reconstructed energy of 1 GeV and pass the shower shape cut which requires $E9/E25 > 0.85$. We reduce the background rate by insuring that the photon candidates are not too close to the projection of any charged tracks on the calorimeter. For $\rho^{\pm}\pi^{\mp}$, the minimum distance requirement is > 2 cm, while for $\rho^0\pi^0$ we require it to be > 5.4 cm. For the $B \rightarrow \rho^+\pi^-$ events the $\gamma\gamma$ invariant mass distribution is presented in Fig. 6.50a, for the pairs with the energy sum of greater than 5 GeV and with the vector sum of transverse momenta greater than 0.75 GeV. The π^0 signal is very clear; the π^0 mass resolution in this sample is 3 to 4 MeV/c^2.

(a) $t = 0$ ps

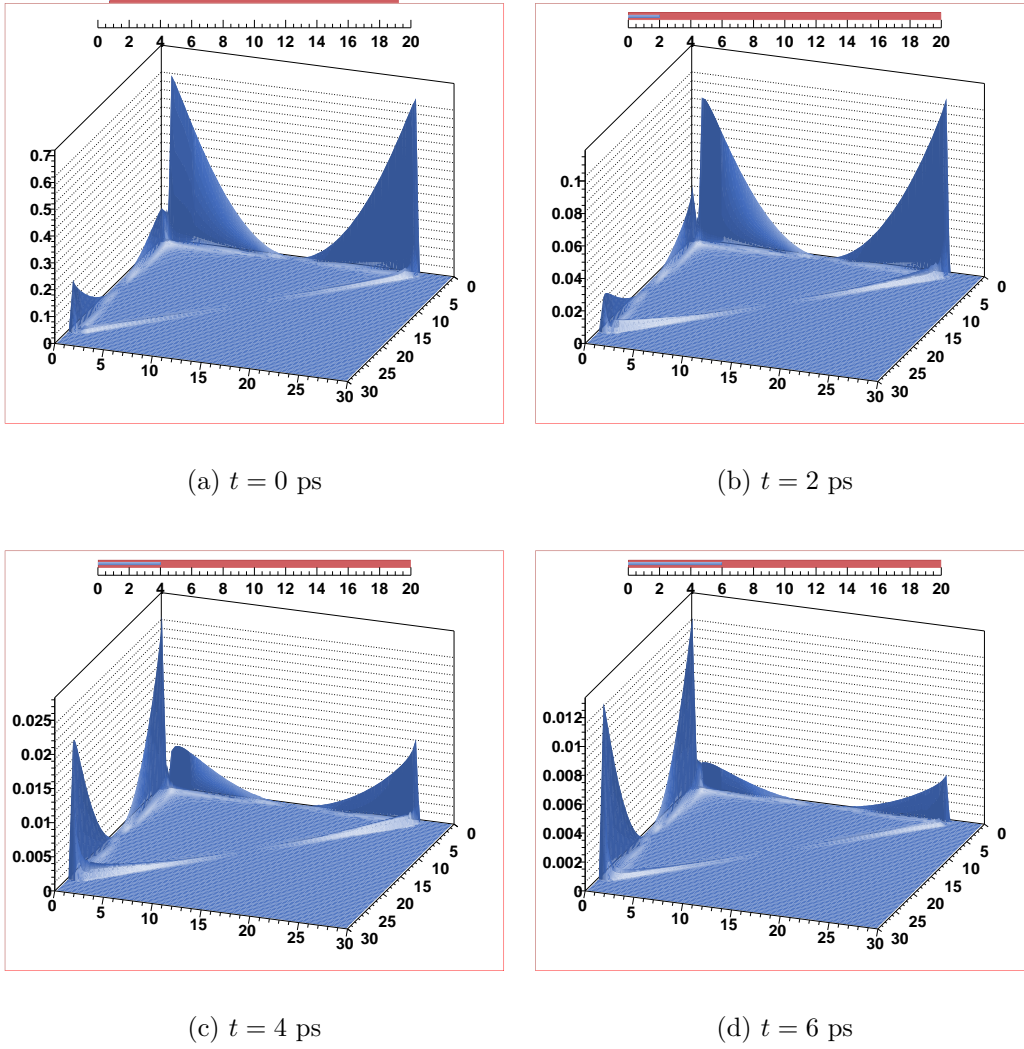(b) $t = 2$ ps

(c) $t = 4$ ps

(d) $t = 6$ ps

Figure 6.49: Evolution of the Dalitz plot versus time

Candidates π^0's are two-photon combinations with invariant masses between 125 and 145 MeV/c^2. The π^0 reconstruction efficiency depends on the distance from beam line and is presented in Fig. 6.50b; the π^0's are taken from the $B^0 \to \rho^\pm \pi^\mp$ events. This simulation was run with a larger than proposed calorimeter so we could view the dependence on radius. (Results on sensitivities are quoted only with the actual geometry.)

We look for events containing a secondary vertex formed by two oppositely charged tracks. One of the most important selection requirements for discriminating the signal from the background is that the events have well measured primary and secondary vertices. We demand that the primary and the secondary vertices be well formed by insisting that $\chi^2/dof < 2$ for their vertex fits. We also make a cut on the B flight significance, L/σ_L, greater than 4: distance between the primary and the secondary vertices divided by the
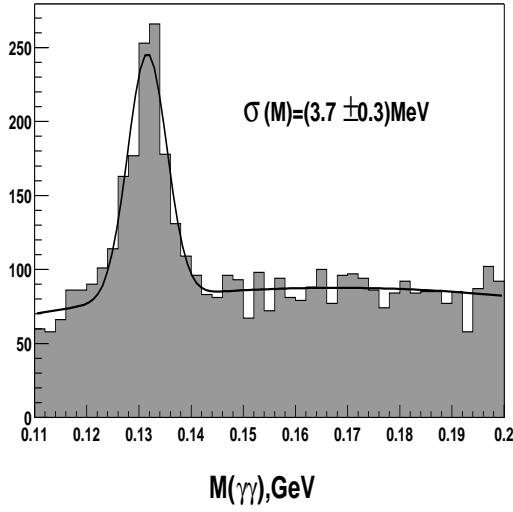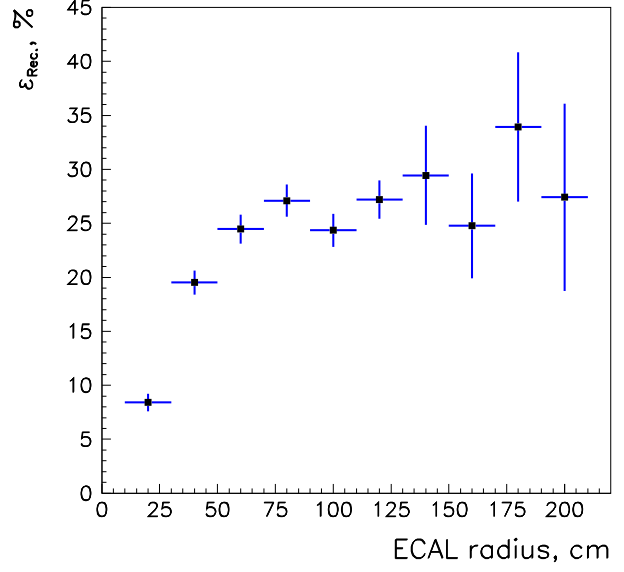
Figure 6.50: The π^0 signal in the $\gamma\gamma$ spectrum from $B^0 \to \rho^+\pi^-$ events (a) and the efficiency of reconstructing the π^0 as a function of distance from the beam line (b). Sample includes a mean of two Poisson distributed non-beauty interactions per beam crossing.

error. The two vertices must also be separated from each other in the plane transverse to the beam. We define $r_{transverse}$ in terms of the primary interaction vertex position (x_P, y_P, z_P) and the secondary vertex position (x_S, y_S, z_S) as $r_{transverse} = \sqrt{(x_P - x_S)^2 + (y_P - y_S)^2}$ and reject events where the secondary vertex is close to the reconstructed primary (see $r_{transverse}$ values in Table 6.7). Furthermore, to insure that the charged tracks do not originate from the primary, we require that both the π^+ and the π^- candidates have an impact parameter with respect to the primary vertex (DCA) greater than $100\mu m$.

When we form the invariant mass of either the $\pi^+\pi^-$ pair or the $\pi^\pm\pi^0$ pair, we require it to be compatible with the ρ mass, that is, between 0.55 and 1.1 GeV/c^2. In addition, we use several kinematics cuts which can greatly reduce the background to $B \to \rho\pi$ while maintaining the signal efficiency. Minimum energy and transverse momentum (p_t) requirements are placed on the three-pion system. The vector sum of p_t's is defined with respect to the B direction which is calculated from the positions of the primary and secondary vertices. We require that p_t^{sum} divided by the scalar sum of the p_t values of all three particles, $(p_t^{\mathrm{sum}}/\Sigma p_t)$, be small. We also make a cut on the B decay time requiring that the B candidate live no more than 5.5 proper lifetimes ($t_{proper}/t_0 < 5.5$). The selection criteria for the two modes are summarized in Table 6.7.

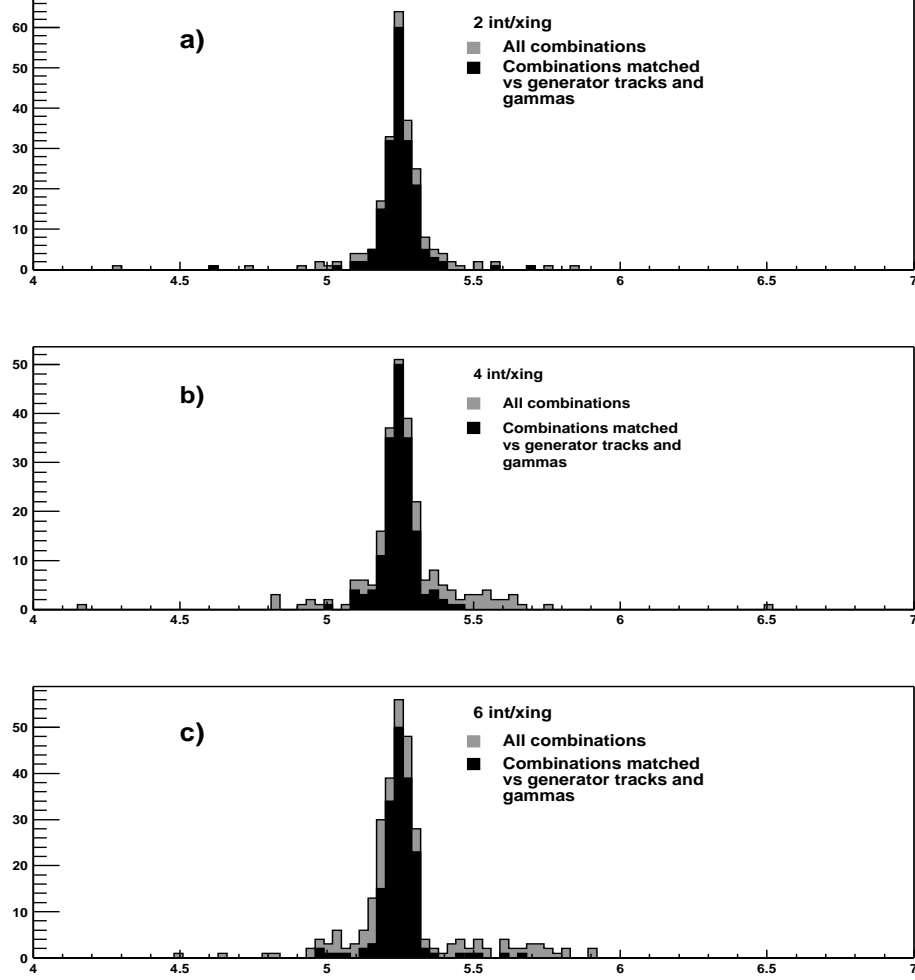The B^0 mass resolution in this sample is in the range 38-42 MeV/c^2.

Figure 6.51: Invariant mass $\pi^+\pi^-\pi^0$, GeV (after cuts) matched vs generator tracks and photons, for 2, 4, and 4 interactions/crossing

The signal interval is taken as $\pm 2\sigma$ around the B mass. The background was obtained by considering the mass interval between 5 and 7 GeV/c^2.

The reconstruction efficiency is $(0.18 \pm 0.02)\%$ for $B^0 \to \rho^0\pi^0$ and $(0.22 \pm 0.02)\%$ for $B^0 \to \rho^\pm\pi^\mp$.

Similar simulation studies were repeated to estimate reconstruction efficiency for the $B^0 \to \rho^+\pi^-$ decay, with the assumption of four and six interactions per crossing. It was found that the ability to reconstruct π^0's at six interactions per crossing does not significantly deteriorate compared to two background interactions per crossing, and the B reconstruction efficiency does not seem to be affected by more than 10%. However, the number of false 3π

Table 6.7: Selection Criteria

Criteria	$\rho^{\pm}\pi^{\mp}$	$\rho^0\pi^0$
Primary vertex criteria	$\chi^2 < 2$	$\chi^2 < 2$
Secondary vertex criteria	$\chi^2 < 2$	$\chi^2 < 2$
$r_{transverse}$ (cm)	0.0146	0.0132
Normalized distance L/σ	> 4	> 4
Distance L, cm	< 5	< 5
DCA of track, μm	> 100	> 100
t_{proper}/t_0	< 5.5	< 5.5
E_{π^+}, GeV	> 4	> 4
E_{π^-}, GeV	> 4	> 4
$p_t(\pi^+)$, GeV/c	> 0.4	> 0.4
$p_t(\pi^-)$, GeV/c	> 0.4	> 0.4
Isolation for γ, cm	> 2.0	> 5.4
E_{π^0}, GeV	> 5	> 9
$p_t(\pi^0)$, GeV/c	> 0.75	> 0.9
$p_t^{\mathrm{sum}}/\Sigma p_t$	< 0.06	< 0.066
m_{π^0}, MeV/c^2	$125 - 145$	$125 - 145$
m_ρ, GeV/c^2	$0.55 - 1.1$	$0.55 - 1.1$

combinations that would pass the cuts increases somewhat as the number of interactions per crossing may go up (see Appendix).

In addition, a check against generator level information was done in order to prove that most of the entries in the B^0 mass region are true $\pi^+\pi^-\pi^0$ combinations coming from the B^0 decay, not false 3π combinations which would mimic the signal. Figure 6.51 illustrate the results of matching against generator level information at two, four, and six interactions per crossing. It is clearly seen that most of the 3π combinations are the correct ones.

We expect to have ~ 500 effective flavor-tagged $\rho^{\pm}\pi^{\mp}$ events and ~ 75 flavor-tagged $\rho^0\pi^0$ events per year (10^7 s). The signal-to-background ratios are 4.1 and 0.3, respectively.

In terms of measuring the angle α following the approach by Quinn and Snyder mentioned above and accounting for the resolutions of the BTeV detector, one would expect from simulation an uncertainty of $\sim 1.5°$ if the true value of α is about $70°$. Since multiple interactions due to different bunch crossings may sligtly affect the reconstruction efficiency while the resolutions remain practically unchanged, the estimate applies to either case of two, four, or six interactions per crossing. Details about this simulation can be found in [16].

6.9   Schedule and Costs

6.9.1   Planning

The planning of the construction of the BTeV Electromagnetic Calorimeter is integrated in the overall BTeV planning. The mechanical structure is expected to be assembled in the C0 Assembly Hall. At least 50% of the Crystal-PMT assemblies will be inserted into the support structure. With our aggressive schedule, up to 90% of the crystals will be in the support structure, while when we allow possible delays in the crystal acqusition, it may be 70%. When the 2009 shutdown starts, the support structure will be moved to the collision hall. We will also place racks of Front-end Boards(FEB's) as well as the light pulsers next to the calorimeter. These electronics will be connected to DCB's and the rest of DAQ system and checked. The rest of the Crystal-PMT assemblies will be inserted into the support structure over the 2010 shutdown.

All 10,000 crystals will be produced and subjected to a quality assurance at BTeV Institutions in 2006-2009. The full calorimeter will be ready to take data for calibration at the end of 2010.

6.9.2   Costs

The full cost of the Electromagnetic calorimeter including contingency is $20.762M. The present cost estimate has been developed over the last several years and the costs were an important consideration in optimizing the design presented in this Technical Design Report.

6.10   Organization

The EMCAL Project Manager Professor Yuichi Kubota from University of Minnessota, appointed by the BTeV co-spokespersons, heads the BTeV Electromagnetic Calorimeter project.

6.10.1   Participating institutes

The BTeV Electromagnetic calorimeter collaboration currently consists of the following institutions :

- Belarussian State University (BSU), Belarussia

- Fermi National Accelerator Laboratory (Fermilab), IL, USA

- Institute for High Energy Physics (IHEP), Protvino, Russia

- University of Minnesota, MN, USA

- Nanjing University, China

- University of Science and Technology of China, China

- Shandong University, China

- Syracuse University, NY, USA

6.10.2 Responsibilities

The work currently being done is to develop the baseline design of EMCAL. The proposed collaborative projects include the following:

- Development of detailed Monte-Carlo simulation code to help understand characteristics EMCAL and R&D results- Fermilab and IHEP

- R&D studies of PWO crystals and PMT's - IHEP, Minnesota, Syracuse and Fermilab

- Complete testing of phototubes - Minnesota and IHEP

- Light Pulser System - IHEP and BSU

- Mechanical design of EMCAL - Fermilab, Minnesota and IHEP

- Electronics - Fermilab

- Development of quality assurance systems to check the optical and radiation hard properties of mass-produced PWO crystals - Chinese institutions and IHEP

Details of the work to be done will be described in Memorandums of Understanding between Fermilab and the collaborative institutions.

The construction of the BTeV Electromagnetic calorimeter is an international project involving institutes all over the world. The construction efforts of the calorimeter are big and it has been decided to distribute the workload among the participating institutes. This organization allows institutional manpower to be engaged at their home institution and thus reduces labor and other associated costs. This strategy also ensures that existing infrastructures in the institutes can be used efficiently and thus investments for necessary laboratory installations can be minimized.

Lead tungstate crystals and phototubes of the Electromagnetic calorimeter need thorough quality control and require numerous acceptance tests. Nanjing University and IHEP will receive the crystals directly from the producers and will carry out necessary crystal quality control program. The phototubes will be tested at Minnesota before installation in the calorimeter.

Front-end electronics will be developed and produced at Fermilab.

Mechanical support will be produced either in Russia or at Fermilab and assembled at Fermilab. Cooling system will be assembled at Fermilab.

Light monitoring system will be developed and assembled in Protvino and then brought to Fermilab. Belarussian State University will participate in this project.

On-line and off-line software for the BTeV electromagnetic calorimeter will be prepared by Fermilab, IHEP, University of Minnesota and Nanjing University.

Bibliography

[1] CMS, The Electromagnetic Calorimeter Project Technical Design Report, CERN/LHCC 97-33, CMS TDR 4 (1997).

[2] ALICE, Technical Design Report of the Photon Spectrometer (PHOS), CERN/LHCC 99-4, ALICE TDR 2 (1999).

[3] T. Brennan *et al.*, "The BTeV electromagnetic calorimeter", Nucl. Instr. and Meth., **A494**, 313–317 (2002).

[4] V.A. Batarin *et al.*, "Development of a Momentum Determined Electron Beam in the 1-45 GeV Range", Preprint IHEP 02-29, Protvino, 2002; e-Print Archive hep-ex/0208012; Nucl. Instr. and Meth., **A510**, 211–218 (2003).

[5] V.A. Batarin *et al.*, "Precision Measurement of Energy and Position Resolutions of the BTeV Electromagnetic Calorimeter Prototype", Preprint IHEP 02-34, Protvino, 2002; e-Print Archive hep-ex/0209055; Nucl. Instr. and Meth., **A510**, 248–261 (2003).

[6] GEANT, Detector Description and Simulation Tool, Computing and Networks Division, CERN

[7] R.Y. Zhu, "Radiation damage in scintillating crystals." Nucl. Instr. and Meth., **A413**, 297–311 (1998).

[8] Private communication with R.Y. Zhu. He told us to measure the uniformity of light collection after we irradiated a small portion along the crystals. If only transmission of light deteriorate in the ragion, since light from any parts of the crystals will pass through this area, the uniformity won't change very much. If the scintillation nmechanism is damaged, on the other hand, light collection from only damaged region will suffer.

[9] I.Azhgirey, I.Kurochkin, V.Talanov, Development of MARS code package for radiation aspects of electronuclear installations design, in: Proc. 15th Conf. on Charged Particles Accelerators, Protvino, 22024 October, 1996, p.74.
I.Azhgirey et al., Calculation of high-energy hadron spectra at the CERN-CEC reference field facility by the MARS'95 and HADRON codes, Nucl. Instr. and Meth., **A408**, 535–542 (1998).

[10] V.A. Batarin *et al.*, "Study of Radiation Damage in Lead Tungstate Crystals Using Intense High Energy Beams", Preprint IHEP 02-35, Protvino, 2002; e-Print Archive hep-ex/0210011; Nucl. Instr. and Meth., **A512**, 484–501 (2003).

[11] V.A. Batarin *et al.*, " LED Monitoring System for the BTeV Lead Tungstate Crystal Calorimeter Prototype", Preprint IHEP 03-32, Protvino, 2003; e-Print Archive physics/0311119; accepted at Nucl. Instr. and Meth.

[12] V.A. Batarin *et al.*, "Comparison of Radiation Damage in Lead Tungstate Crystals Under Pion and Gamma Irradiation", Preprint IHEP 04-03, Protvino, 2004; e-Print Archive physics/0312063; NIM, **A530**, 286-292 (2004).

[13] V.A. Kachanov et al., "Light source for energy stabilization of calorimeter detectors based on photodetectors," NIM, **A314**, 215-218 (1992).

[14] T. Tope, "BTeV EM Calorimeter Thermal Analysis Report," BTeV doc 1050

[15] A. E. Snyder and H. R. Quinn. Measuring cp asymmetry in b → rho pi decays without ambiguities. *Phys. Rev.*, **D48**, 2139–2144 (1993).

[16] M. Rovere, "Measuring α with $B^0 \rightarrow \rho\pi$ in the BTeV experiment", BTeV-doc-3038, (2004).